

# Simulation of mixed-mode fracture using SPH particles with an embedded fracture process zone

Yingnan Wang<sup>1,2</sup> | Hieu T. Tran<sup>1,2</sup> | Giang D. Nguyen<sup>3</sup> |  
Pathegama G. Ranjith<sup>2</sup> | Ha H. Bui<sup>1,2</sup> 

<sup>1</sup>Monash Computational Geomechanics (MCG) Lab, Monash University, Melbourne, Victoria, Australia

<sup>2</sup>Department of Civil Engineering, Monash University, Melbourne, Victoria, Australia

<sup>3</sup>School of Civil, Environmental & Mining Engineering, University of Adelaide, Adelaide, South Australia, Australia

## Correspondence

Ha H. Bui, Department of Civil Engineering, Monash University, R126, 23 College Walk, Clayton, Melbourne, Victoria 3800, Australia.  
Email: ha.bui@monash.edu

## Funding information

Australian Research Council through Discovery Projects, Grant/Award Numbers: DP190102779, DP170103793, FT140100408, DP160100775

## Summary

This paper focuses on the modelling of mixed-mode fracture using the conventional smoothed particle hydrodynamics (SPH) method and a mixed-mode cohesive fracture law embedded in the particles. The combination of conventional SPH and a mixed-mode cohesive model allows capturing fracture and separation under various loading conditions efficiently. The key advantage of this framework is its capability to represent complex fracture geometries by a set of cracked SPH particles, each of which can possess its own mixed-mode cohesive fracture with arbitrary orientations. Therefore, this can naturally capture complex fracture patterns without any predefined fracture topologies. Because a characteristic length scale related to the size of the fracture process zone is incorporated in the constitutive formulation, the proposed approach is independent from the spatial discretisation of the computational domain (or mesh independent). Furthermore, the anisotropic fracture responses of materials can be naturally captured thanks to the orientation of the fracture process zone embedded at the particle level. The performance of the proposed approach demonstrates its potentials in modelling mixed-mode fracture of rocks and similar quasi-brittle materials.

## KEY WORDS

cohesive fracture law, mixed-mode, regularisation, rock fracture, smoothed particle hydrodynamics (SPH)

## 1 | INTRODUCTION

An understanding of rock fracture under complex loading conditions is important in civil engineering applications and energy exploration activities such as tunnel construction, oil and gas extraction and underground water transport. This has triggered numerous research efforts through analytical studies of rock fractures, which can be traced back to the invention of linear elastic fracture mechanics in the past century (Griffith and Eng and Irwin<sup>1,2</sup>). Since then, numerous criteria including the maximum stress criterion, the minimum strain energy density criterion and the maximum energy release rate criterion, are well established and applied for predicting mixed-mode fracture initiation and propagation.<sup>3</sup> On the other hand, a significant amount of research has been conducted on experimental analysis of crack growth and propagation under variable loading conditions.<sup>4</sup> Various test methods have been used by researchers for determining

the mixed-mode fracture toughness of brittle materials such as rocks for all mode mixtures from pure mode I to pure mode II. They include 3-point bending test with semicircular specimen,<sup>5,6</sup> diametrical compression test with notch Brazilian disc,<sup>7,8</sup> 3- or 4-point bending with single-edge-cracked rectangular beam<sup>9,10</sup> and compact tension and shear test.<sup>11,12</sup>

It has been well known that it is challenging for mesh-based methods like the finite element methods (FEMs) to capture the fracture and separation of materials.<sup>13</sup> The capabilities of the FEMs can be greatly extended by different enhancements, like the extended FEM<sup>14–18</sup> and similar approaches such as strong discontinuity approach<sup>19–25</sup> and enhanced assumed strain.<sup>26–29</sup> However, they are usually mathematically complicated while still not being able to resolve all inherent issues of the FEMs in handling severe mesh distortion and fragmentation. On the other hand, with the advances of computing powers, discrete models such as discrete element method and hybrid continuum-discrete methods show great feasibility in modelling large deformation and fragmentation problems.<sup>30–35</sup> However, those models are still limited to laboratory-size tests that only involve a limited number of particles due to its discrete nature of detecting particle interaction, which hinders the large-scale practical application of discrete methods.

An alternative approach to model fracture propagation and fragmentation is mesh-free continuum methods. These methods can achieve numerical solutions without using any computational grid, thus are highly flexible in modelling large deformation problems while being computationally much cheaper than discrete element method. One example of mesh-free methods is the smoothed particle hydrodynamics (SPH) method. Invented by Gingold and Monaghan<sup>36</sup> and Lucy,<sup>37</sup> SPH has been successfully applied to a wide range of engineering applications such as large deformation and failure of geomaterials,<sup>38–40</sup> slope failures,<sup>41–43</sup> granular flows and landslides,<sup>44–49</sup> soil-structure interaction,<sup>50–54</sup> coupled soil-water problems<sup>55–57</sup> and among many others.<sup>49</sup> SPH combined with a traditional constitutive model such as elastoplastic or coupled elastoplastic and damage models has also been extended to rock fractures in literature.<sup>58–60</sup> Although those constitutive models could successfully capture the macro-behaviour of rocks such as stiffness degradation, irreversible deformation and the fracture processes such as initiation, propagation and fracture patterns under various loading conditions, the deformation of a particle in these models is assumed to be homogeneous, thereby neglecting the existence of a high gradient of deformation across the localisation band during the nonlinear phases of rock fracture. In addition, those models fail to account for the characteristics of the localisation zone such as size, fracture orientation and evolution of inelastic behaviour, together with the material behaviour outside the zone. As a consequence, the localisation of deformation in these models depends highly on the resolution of discretisation, which is also called mesh dependence.

In addition, the conventional SPH suffers from tensile instability when being applied to problems involved tensile stress loading. To address this issue, a simple technique, namely, the artificial stress method,<sup>61,62</sup> was proposed and demonstrated to be sufficient to completely remove this tensile instability.<sup>50</sup> Together with the artificial stress technique, the SPH method has demonstrated its simplicity, versatility and efficiency for solving complex problems with reference to field-scale applications. As an alternative approach to deal with the tensile instability, Taylor SPH method that combines the corrected SPH technique,<sup>63</sup> the stress point approach<sup>64,65</sup> and the Taylor-Galerkin time integration scheme<sup>66,67</sup> has been developed recently for shock wave propagation problems.<sup>68,69</sup> This approach has been recently extended to model pure mode-I rock fracture problems by incorporating a new continuum size-dependent constitutive model with embedded cohesive fracture process zone (FPZ).<sup>70–72</sup> A key feature of the new constitutive model is the inclusion of additional kinematic enhancement to account for the high gradient of deformation across the fracture plane beyond onset of fracture. In addition, size effects are intrinsically captured thanks to the inclusion of the characteristic length parameter in the model formulation, which helps eliminate the mesh dependency in numerical analysis of boundary value problems. The combination of Taylor SPH and the new constitutive model<sup>72</sup> has demonstrated its capability to capture the experimentally observed size-dependent behaviour of rock fracture under pure mode I loading conditions. Thanks to the characteristic length scale embedded in the constitutive model, the proposed numerical framework is independent with the spatial discretisation of the computational domain (or mesh independent). This success, as a proof of concept, demonstrates the capabilities and potentials of the SPH with a FPZ idealised as a cohesive model embedded in the particles to capture rock fracture and fragmentation. However, the previous work utilised mode I constitutive model and thus could only capture mode I rock fracture SPH. Furthermore, the Taylor SPH method employs two sets of particles with a two-step Taylor time integration scheme and requires special treatments for free-surface boundary conditions, resulting in a relatively complicated model for simulating rock fracture problems. Therefore, further works are required to improve the constitutive model as well as to simplify the Taylor SPH method to capture rock fracture and fragmentation under mixed-mode loading conditions.

In this study, the SPH-based numerical framework, previously reported in Wang et al.<sup>72</sup> to model pure mode I rock fracture, is further developed to fully capture rock fracture under mixed-mode loading conditions. However, different from the previous study,<sup>72</sup> the conventional SPH framework with tensile instability treatment<sup>50</sup> instead of the Taylor SPH method is adopted in this study. The key advantages of this approach include the following: (i) it does not require an extra set of stress particles, thus in principle, can reduce the overall computational cost, and (ii) it does not require any prescribed stress boundary condition on the free surface, thus is more computationally efficient to handle complex applications. In conjunction with the conventional SPH framework, a size-dependent constitutive model with an embedded mixed-mode cohesive fracture is employed for describing the stress states of rock under a wide range of loading conditions. Different from the previous work in Wang et al.<sup>72</sup> which focuses on the pure mode I fracture, the FPZ in this study is described by a mixed-mode cohesive fracture law for capturing the plastic and damage evolutions of material under various loading conditions. The combination of these two approaches enables the proposed numerical framework to represent fracture geometries by a set of damaged SPH particles, each of which possesses its own FPZ with arbitrary orientations, therefore can naturally capture complex fracture patterns without any predefined topology. The rest of paper is organised as follows. The general SPH framework for simulating rock materials is presented in Section 2. The concept of size-dependent constitutive model and details of model formulations are then explained in Section 3. This is followed by an implicit implementation algorithm of the constitutive model and demonstrations of model behaviour at the constitutive level under complex loading conditions in Section 4. Section 5 presents three applications to examine its capability in predicting mixed-mode rock fractures. Finally, a conclusion drawn from this study is summarised in Section 6.

## 2 | SPH MODELLING FOR ROCK

### 2.1 | SPH equations of motion for rock

SPH is a purely Lagrangian mesh-free method without underlying grids. The computational domain in SPH is discretised into a finite number of particles that carry their own field variables such as density, velocity and stress and move according to the governing equations.<sup>39</sup> For rock fracture problems, the governing equations consist of mass and momentum conservation equations and a constitutive relationship that links stresses to strains through a set of equations as follows:

$$\frac{D\rho}{Dt} = -\rho \nabla \cdot \mathbf{v}, \quad (1)$$

$$\frac{D\mathbf{v}}{Dt} = \frac{1}{\rho} \nabla \cdot \boldsymbol{\sigma} + \mathbf{b}, \quad (2)$$

$$\frac{D\boldsymbol{\sigma}}{Dt} = \mathbf{D}_{ef} : \dot{\boldsymbol{\epsilon}}, \quad (3)$$

where  $\rho$  is the material density;  $\mathbf{v}$  is the velocity vector;  $\boldsymbol{\sigma}$  is the stress tensor;  $\mathbf{b}$  is the vector component of acceleration due to external forces;  $\mathbf{D}_{ef}$  is the material stiffness matrix;  $D(\cdot)/Dt$  is the material derivative and  $\dot{\boldsymbol{\epsilon}}$  is the strain rate tensor, which can be calculated by velocity through the following kinematic relation:

$$\dot{\boldsymbol{\epsilon}} = \left[ \nabla \cdot \mathbf{v} + (\nabla \cdot \mathbf{v})^T \right] / 2. \quad (4)$$

In the SPH method, the approximation of the mass and momentum conservation equations are conducted in two consecutive steps: kernel approximation and particle approximation. In the kernel approximation step, a field function  $f(x)$  and its spatial derivatives  $\nabla f(x)$  are approximated by integral equations that involve a smoothing function and its derivatives as follows, respectively:

$$\langle f(\mathbf{x}) \rangle = \int_{\Omega} f(\mathbf{x}') W(\mathbf{x} - \mathbf{x}', h) d\mathbf{x}', \quad (5)$$

$$\langle \nabla f(\mathbf{x}) \rangle = - \int_{\Omega} f(\mathbf{x}') \cdot \nabla W(\mathbf{x} - \mathbf{x}', h) d\mathbf{x}', \quad (6)$$

where the angle bracket  $\langle \rangle$  represents the kernel approximation operator,  $W(\mathbf{x} - \mathbf{x}', h)$  is the smoothing (or kernel) function,  $h$  is the smoothing length defined an effective domain  $\Omega$  of the smoothing function and  $\nabla W(\mathbf{x} - \mathbf{x}', h)$  is the derivative of  $W$  with respect to  $\mathbf{x}'$  and will be referred to as  $\nabla W$  throughout the manuscript.

The particle approximation, on the other hand, consists in converting the integral equations, that is, Equations 5 and 6, into discretised forms of summation over all particles  $\mathbf{x}_j$  located within the support domain of a given particle at  $\mathbf{x}_i$ . Accordingly, the particle approximation of a field function and its spatial derivative can be written in the following forms as

$$f(\mathbf{x}_i) = \sum_{j=1}^N \frac{m_j}{\rho_j} f(\mathbf{x}_j) W_{ij}, \quad (7)$$

$$\nabla f(\mathbf{x}_i) = \sum_{j=1}^N \frac{m_j}{\rho_j} f(\mathbf{x}_j) \cdot \nabla W(\mathbf{x}_i - \mathbf{x}_j, h), \quad (8)$$

where  $W_{ij} = W(|\mathbf{x}_i - \mathbf{x}_j|, h)$  and  $\nabla W_{ij} = \left( \frac{\mathbf{x}_i - \mathbf{x}_j}{|\mathbf{r}|} \right) \frac{\partial W_{ij}}{\partial r}$ .

with  $\nabla W_{ij}$  denote the gradient of kernel the function  $W_{ij}$  evaluated at the location  $\mathbf{x}_i$ ;  $|\mathbf{r}| = |\mathbf{x}_i - \mathbf{x}_j|$  is the relative distance between particles  $i$  and  $j$ ;  $N$  is the total number of neighbouring particles of  $i$  within its supporting domain; and  $m_j/\rho_j$  is the volume of particle  $j$ .

The SPH approximation of governing equations can be now derived using Equations 7 and 8. Several different approaches to derive SPH approximations of governing equations by means of some transformations are available in the literature. In this study, the most commonly used formulations of mass and momentum equations are adopted and written as

$$\frac{D\rho_i}{Dt} = \sum_{j=1}^N m_j (\mathbf{v}_i - \mathbf{v}_j) \cdot \nabla W_{ij}, \quad (9)$$

$$\frac{D\mathbf{v}_i}{Dt} = \sum_{j=1}^N m_j \left( \frac{\boldsymbol{\sigma}_i + \boldsymbol{\sigma}_j}{\rho_i \rho_j} + \mathbf{C}_{ij} \right) \cdot \nabla W_{ij} + \mathbf{b}_i, \quad (10)$$

$$\frac{D\boldsymbol{\sigma}_i}{Dt} = \mathbf{D}_{\text{ef}} : \left[ \frac{1}{2} \sum_{j=1}^N \frac{m_j}{\rho_j} (\mathbf{v}_j - \mathbf{v}_i) \cdot \nabla W_{ij} + \frac{1}{2} \left( \sum_{j=1}^N \frac{m_j}{\rho_j} (\mathbf{v}_j - \mathbf{v}_i) \cdot \nabla W_{ij} \right)^T \right], \quad (11)$$

where  $\mathbf{C}_{ij}$  is a stabilisation term consisting of artificial viscosity and artificial stress.<sup>39</sup> The artificial viscosity is proportional to the sound speed of a material and acts as a damping term to regularise stress fluctuation, whereas the artificial stress is usually utilised to prevent particles clumping under tensile stress. Examples of large-scale slope failure in Bui et al.<sup>39,41</sup> demonstrated that the tensile instability problem can be completely removed by adding the stabilisation term. In this study, the artificial viscosity is the only used stabilisation term to regularise the strong shock wave propagation in hard rocks. This is because the sound speed that propagates in hard rocks is often much faster than that in soft rocks or, in order words, the elastic Young's modulus of hard rocks is often very large. This results in larger influence of artificial viscosity in the momentum equation and thus mitigating the tensile instability problem. However, when it comes to the examples related to soft rocks, both the artificial viscosity and artificial stress have to be adopted as the artificial viscosity is not enough to mitigating the tensile instability problem. The inclusion of artificial stress helps preventing particles from getting closer by applying a repulsive force between neighbouring particles when they are subjected to

tensile loading. The constant parameters for the artificial viscosity in this study are chosen to be 0.5 and 0 for the terms associated with the linear and quadratic in the velocity divergence, respectively, whereas the constant parameter for the artificial stress is selected as 0.2.

## 2.2 | The correction of kernel gradient

The above SPH approximation formulations in principle can achieve a second-order accuracy. However, this is not always the case, especially when the material undergoes large deformation that leads to highly disorder particle configuration. The problem can be severe when it comes close to the boundary where the kernel approximation is truncated by the boundary, although this is also an advantage of SPH that allows the method to automatically handle free-surface boundary conditions in many applications.<sup>73</sup> To address this issue, the SPH corrective technique originally developed by Chen et al.<sup>63</sup> is adopted in this study. The approach allows both the kernel and its gradient approximations to be corrected by means of the Taylor series expansion. As the discrete forms of derivatives of the governing equations all make use of the kernel gradient, the correction of kernel gradient is a key to improving the solution. Therefore, only correction of kernel gradient is described here, which starts by rewriting the gradient of a field function  $\nabla f(\mathbf{x})$  to the following form:

$$\nabla f(\mathbf{x}) = \nabla f(\mathbf{x}) - f(\mathbf{x}). \quad (12)$$

Transforming Equation 12 into its continuous integral form using Equation 6 results in

$$\langle \nabla f(\mathbf{x}) \rangle = - \int_{\Omega} f(\mathbf{x}') \nabla W d\mathbf{x}' + f(\mathbf{x}) \int_{\Omega} \nabla W d\mathbf{x}'. \quad (13)$$

By applying the Taylor series expansion to  $f(\mathbf{x}')$  up to the second order accuracy, the first term on the right-hand side of Equation 13 becomes

$$\int_{\Omega} f(\mathbf{x}') \nabla W d\mathbf{x}' = f(\mathbf{x}) \int_{\Omega} \nabla W d\mathbf{x}' + \left[ \int_{\Omega} (\mathbf{x}' - \mathbf{x}) \nabla W d\mathbf{x}' \right] \frac{\partial f(\mathbf{x})}{\partial \mathbf{x}} + O(h^2). \quad (14)$$

Substituting Equation 14 into Equation 13 gives

$$\langle \nabla f(\mathbf{x}) \rangle = - \left[ \int_{\Omega} (\mathbf{x}' - \mathbf{x}) \nabla W d\mathbf{x}' \right] \frac{\partial f(\mathbf{x})}{\partial \mathbf{x}} + O(h^2). \quad (15)$$

The discrete form of Equation 15 at a particle  $i$  can be straightforwardly written as

$$\nabla f(\mathbf{x}_i) = \left[ \sum_{j=1}^N \frac{m_j}{\rho_j} (\mathbf{x}_j - \mathbf{x}_i) \nabla W_{ij} \right] \frac{\partial f(\mathbf{x})}{\partial \mathbf{x}_i} + O(h^2). \quad (16)$$

It can be seen from Equation 16 that the particle approximation for the gradient of a function can achieve a second-order accuracy if and only if  $\sum_{j=1}^N \frac{m_j}{\rho_j} (\mathbf{x}_j - \mathbf{x}_i) \nabla W_{ij} = \begin{pmatrix} 1 & 0 \\ 0 & 1 \end{pmatrix}$ . However, this requirement cannot be always satisfied especially when particles are located near the boundaries. This issue can be resolved by replacing original kernel gradient  $\nabla W_{ij}$  in Equation 16 by a corrective kernel gradient  $\nabla W_{ij}^C$  as follows:

$$\nabla W_{ij}^C = \mathbf{L}(\mathbf{x}_i) \nabla W_{ij}, \quad (17)$$

where the normalisation matrix  $\mathbf{L}(\mathbf{x}_i)$  can be defined as

$$\mathbf{L}(\mathbf{x}_i) = \begin{pmatrix} \sum_{j=1}^N \frac{m_j}{\rho_j} (x_j - x_i) \nabla_{x_i} W_{ij} & \sum_{j=1}^N \frac{m_j}{\rho_j} (x_j - x_i) \nabla_{y_i} W_{ij} \\ \sum_{j=1}^N \frac{m_j}{\rho_j} (y_j - y_i) \nabla_{x_i} W_{ij} & \sum_{j=1}^N \frac{m_j}{\rho_j} (y_j - y_i) \nabla_{y_i} W_{ij} \end{pmatrix}^{-1}. \quad (18)$$

By substituting Equations 17 and 18 to Equation 16, it can be straightforwardly seen that the SPH approximation for the gradient of a function is of second-order accuracy, and thus resolving the general problems of particle deficiency at the boundaries in the traditional SPH. Therefore, the corrective kernel gradient instead of the conventional one is applied in this study, and the governing equations can be rewritten as shown below

$$\frac{D\rho_i}{Dt} = \sum_{j=1}^N m_j (\mathbf{v}_i - \mathbf{v}_j) \cdot \nabla W_{ij}^C, \quad (19)$$

$$\frac{D\mathbf{v}_i}{Dt} = \sum_{j=1}^N m_j \left( \frac{\boldsymbol{\sigma}_i + \boldsymbol{\sigma}_j}{\rho_i \rho_j} + C_{ij} \right) \cdot \nabla W_{ij}^C + \mathbf{b}_i, \quad (20)$$

$$\frac{D\boldsymbol{\sigma}_i}{Dt} = \mathbf{D}_{\text{ef}} : \left[ \frac{1}{2} \sum_{j=1}^N \frac{m_j}{\rho_j} (\mathbf{v}_j - \mathbf{v}_i) \cdot \nabla W_{ij}^C + \frac{1}{2} \left( \sum_{j=1}^N \frac{m_j}{\rho_j} (\mathbf{v}_j - \mathbf{v}_i) \cdot \nabla W_{ij}^C \right)^T \right]. \quad (21)$$

## 2.3 | Time integration

The above set of differential equations in the form of SPH discretisation (19–21) can be integrated with standard techniques such as the second-order accurate LeapFrog (LF), predictor–corrector and second- or fourth-order Runge–Kutta schemes. In this study, LF integration method is applied due to its low memory storage requirement in the computation process and high efficiency for one force evaluation per step.<sup>74</sup> In the LF method, state variables of each SPH particle such as density, velocity and stress are updated at mid-steps in time, whereas its position is updated at full-time steps. Hence, at the beginning of the computation, the state variables need to be advanced to the mid-time step using the following equations:

$$\rho_{1/2} = \rho_0 + \frac{\Delta t}{2} \left( \frac{D\rho}{Dt} \right)_0, \quad (22)$$

$$\mathbf{v}_{1/2} = \mathbf{v}_0 + \frac{\Delta t}{2} \left( \frac{D\mathbf{v}}{Dt} \right)_0, \quad (23)$$

$$\boldsymbol{\sigma}_{1/2} = \boldsymbol{\sigma}_0 + \frac{\Delta t}{2} \left( \frac{D\boldsymbol{\sigma}}{Dt} \right)_0. \quad (24)$$

Subsequently, the above-stated variables are updated in a full-time increment using the following equations:

$$\rho_{n+1/2} = \rho_{n-1/2} + \Delta t \left( \frac{D\rho}{Dt} \right)_n, \quad (25)$$

$$\mathbf{v}_{n+1/2} = \mathbf{v}_{n-1/2} + \Delta t \left( \frac{D\mathbf{v}}{Dt} \right)_n , \quad (26)$$

$$\boldsymbol{\sigma}_{n+1/2} = \boldsymbol{\sigma}_{n-1/2} + \Delta t \left( \frac{D\boldsymbol{\sigma}}{Dt} \right)_n , \quad (27)$$

where  $(\frac{D\rho}{Dt})_n$ ,  $(\frac{D\mathbf{v}}{Dt})_n$  and  $(\frac{D\boldsymbol{\sigma}}{Dt})_n$  are calculated by means of density( $\rho_n$ ), velocity ( $\mathbf{v}_n$ ) and stress ( $\boldsymbol{\sigma}_n$ ) at time step  $n$ , which are updated as follows:

$$\rho_n = \rho_{n-1/2} + \frac{\Delta t}{2} \left( \frac{D\rho}{Dt} \right)_{n-1} , \quad (28)$$

$$\mathbf{v}_n = \mathbf{v}_{n-1/2} + \frac{\Delta t}{2} \left( \frac{D\mathbf{v}}{Dt} \right)_{n-1} , \quad (29)$$

$$\boldsymbol{\sigma}_n = \boldsymbol{\sigma}_{n-1/2} + \frac{\Delta t}{2} \left( \frac{D\boldsymbol{\sigma}}{Dt} \right)_{n-1} . \quad (30)$$

Finally, the locations of particles are updated at a full-time step using the velocity at the mid-time step as follows:

$$\mathbf{x}_{n+1} = \mathbf{x}_n + \Delta t \times \mathbf{v}_{n+1/2} . \quad (31)$$

In order to maintain the stability of the LF integration, the time step  $\Delta t$  must satisfy a certain condition, which is proportional to the smoothing length ( $h$ ) adopted in the computation. In this study, the time step is determined by the following condition:

$$\Delta t \leq C_{\text{cour}} \left( \frac{h}{c} \right) , \quad (32)$$

where  $C_{\text{cour}}$  is Courant number, which is chosen as 0.1;  $c = \sqrt{E/\rho}$  is sound speed with  $E$  being the Young's modulus of the material.

### 3 | A MIXED-MODE CONTINUUM CONSTITUTIVE MODEL FOR ROCK FRACTURE

In this section, a continuum-based constitutive model taking into account size effect is presented for rock fracture application under mixed-mode loading conditions. The mixed-mode fracture behaviour of rock material is governed by a mixed-mode cohesive fracture law, although the kinematic enrichment to accommodate this cohesive fracture law is originated from the double-scale approach for strain localisation problems.<sup>75,76</sup> The basic ideas of the double-scale framework and its key formulations are presented first, followed by the introduction of a mixed-mode cohesive fracture law. The implementation algorithm for the constitutive model is also provided at the end of this section.

#### 3.1 | Double-scale framework

In the traditional constitutive model, the deformation of a representative volume element (RVE) is assumed to be homogeneous. However, this assumption is not always appropriate for rock fracture problems in which a strong variation of strain exists across the FPZ due to the presence of discontinuity such as joints and fractures. In that case, it is utmost important to employ a constitutive model accounting for the two distinct responses of material inside of

localised zone and outside it. There have been some models that can correctly capture the behaviour inside and outside the localised zone by introducing kinematic enrichments to its constitutive structure.<sup>75–80</sup> In this study, the double-scale approach developed by Nguyen et al.<sup>75,76</sup> and further improved in Nguyen and Bui<sup>81</sup> is adopted for mixed-mode rock fracture applications, due to its advantages in automatically giving the derived constitutive models an intrinsic length scale associated with localised failure and/or fracture. This approach has been employed with success in SPH to simulate rock fracture under pure mode I loading,<sup>72</sup> complex soil cracking<sup>82,83</sup> and in FEM for simulating failure in rocks and concrete,<sup>84–87</sup> and fibre-reinforced aerospace composites,<sup>88</sup> thanks to its simplicity, versatility and computational efficiency in modelling complex cracking phenomena. This approach is now extended to modelling mixed-mode fracture in rocks using a mixed-mode cohesive fracture law for capturing postlocalisation behaviour of the material. The below formulation is standard and generic for this size-dependent constitutive model and hence provided only for the sake of completeness to make this paper a standalone one.

In the double-scale model, the RVE ( $\Omega$ ) is considered as a composite material comprising a FPZ ( $\Omega_i$ ) and outside bulk ( $\Omega_o$ ); see Figure 1A. It is generally assumed that energy dissipation only takes place inside FPZ, while the outside material remains elastic. The double-scale model is only activated when the fracture is detected. In other words, the element is initially treated as homogenous and elastic before the fracture is triggered. After that point, the fracture plane characterised by fracture direction  $\mathbf{n}$  (Figure 1A) is formed, dividing the RVE into two zones. The local behaviour of the FPZ and the surrounding zone under various loading conditions are described separately. To be more specific, material within the FPZ undergoes inelastic loading behaviour with an increasing strain, indicating energy dissipation during the fracture development, while the outside material is under elastic unloading, shown as in Figure 1B. All these features will contribute to a macroscopic stress-strain relationship over the whole volume element through energy conservation and traction continuity conditions. The name “double scale” is used to indicate the distinction between the behaviour of the localisation zone at the mesoscale, and the macro-volume element containing it.

In the double-scale approach, the overall (or macro) strain rate can be decomposed into the strain rate inside and outside FPZ with its volume contribution to macro-strain rate, expressed as

$$\dot{\epsilon} = \eta \dot{\epsilon}_{\text{in}} + (1 - \eta) \dot{\epsilon}_{\text{out}}, \quad (33)$$

where  $\eta = \frac{\Omega_i}{\Omega} = h/H$  is the volume fraction of FPZ.

The strain rate inside the FPZ can be approximated by the rate of the displacement jump  $[\dot{\mathbf{u}}]$  in the global coordinate system:<sup>89,90</sup>

$$\dot{\epsilon}_{\text{in}} \approx \frac{1}{h} \mathbf{n} [\dot{\mathbf{u}}], \quad (34)$$

where  $\mathbf{n}$  denotes the normal vector to the localised surface. The behaviour of material inside FPZ is described by a cohesive fracture law, which defines a relationship between the rate of traction and the rate of displacement jump across the localization zone. The detailed formulations and implementation algorithm of cohesive fracture law will be discussed in the Section 3.2, and its generic formulations in the global coordinate system can be written as

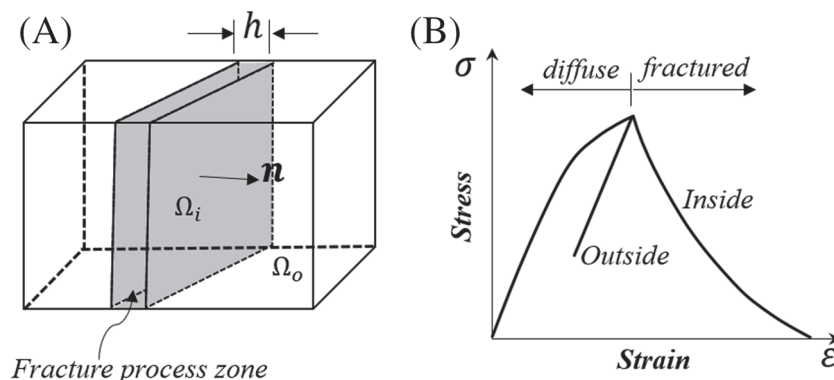


**FIGURE 1** A size-dependent constitutive model: (A) fracture process zone surrounded by an elastic bulk and (B) corresponding stress-strain responses inside and outside the fracture process zone (after Nguyen et al.<sup>76</sup>)

$$\dot{\mathbf{t}}_{\text{in}} = \mathbf{K}^t [\dot{\mathbf{u}}], \quad (35)$$

where  $\mathbf{K}^t = \mathbf{R}^T \mathbf{K}_c^t \mathbf{R}$  is the tangent stiffness matrix of FPZ in the global coordinate;  $\mathbf{K}_c^t$  is the local tangent stiffness matrix and  $\mathbf{R}$  is the rotational matrix from the global to local coordinate systems;  $\dot{\mathbf{t}}_{\text{in}}$  denotes the rate of traction at the boundary of FPZ in the global coordinate system. Different from the behaviour of inside material, the behaviour of bulk material outside FPZ is described by Hooke's law, defined as

$$\dot{\boldsymbol{\sigma}}_{\text{out}} = \mathbf{a}_0 \dot{\boldsymbol{\varepsilon}}_{\text{out}} = \frac{1}{(1-\eta)} \mathbf{a}_0 \left( \dot{\boldsymbol{\varepsilon}} - \frac{\eta}{h} \mathbf{n} [\dot{\mathbf{u}}] \right), \quad (36)$$

in which  $\mathbf{a}_0$  is the elastic stiffness matrix, expressed in terms of Young's modulus and Poisson's ratio. Because the material behaviour of two distinct regions (FPZ and bulk material) are determined, the next step is to connect those two regions and derive an overall (macro) stress-strain relationship for the element volume  $\Omega$ . This can be achieved by using Hill–Mandel condition,<sup>91</sup> in which the virtual work done by macro-stress–strain rate has to equilibrate the total work produced by stress–strain rate inside and outside FPZ

$$\boldsymbol{\sigma}^T \dot{\boldsymbol{\varepsilon}} = (1-\eta) \boldsymbol{\sigma}_{\text{out}}^T \dot{\boldsymbol{\varepsilon}}_{\text{out}} + \eta \boldsymbol{\sigma}_{\text{in}}^T \dot{\boldsymbol{\varepsilon}}_{\text{in}}. \quad (37)$$

Substituting Equations 33 and 34 into Equation 38 and rearranging the equation, we can get

$$(1-\eta) (\boldsymbol{\sigma}^T - \boldsymbol{\sigma}_{\text{out}}^T) \dot{\boldsymbol{\varepsilon}}_{\text{out}} + \frac{\eta}{h} (\mathbf{t}^T - \mathbf{t}_{\text{in}}^T) [\dot{\mathbf{u}}] = 0. \quad (38)$$

From the above equation, it can be seen that this condition can always be fulfilled for any  $\dot{\boldsymbol{\varepsilon}}_{\text{out}} [\dot{\mathbf{u}}]$  when (1) the macro-stress coincides with the outside stress

$$\boldsymbol{\sigma} = \boldsymbol{\sigma}_{\text{out}} \quad (39)$$

and (2) the traction continuity at the boundary of fracture plane is met

$$\mathbf{n}^T \boldsymbol{\sigma} = \mathbf{t}_{\text{in}}. \quad (40)$$

Combining Equations 36 and 39 and the condition  $h \rightarrow 0$  for rock fracture applications, the macro-stress–strain relationship can be obtained as

$$\dot{\boldsymbol{\sigma}} = \dot{\boldsymbol{\sigma}}_{\text{out}} = \mathbf{a}_0 \left( \dot{\boldsymbol{\varepsilon}} - \frac{1}{H} \mathbf{n} [\dot{\mathbf{u}}] \right), \quad (41)$$

in which the rate of displacement jump  $[\dot{\mathbf{u}}]$  can be calculated by combining Equation 35 and Equations 40 and 41, leading to

$$[\dot{\mathbf{u}}] = \left( \frac{1}{H} \mathbf{n}^T \mathbf{a}_0 \mathbf{n} + \mathbf{K}^t \right)^{-1} \mathbf{n}^T \mathbf{a}_0 \dot{\boldsymbol{\varepsilon}} = \mathbf{C}^{-1} \mathbf{n}^T \mathbf{a}_0 \dot{\boldsymbol{\varepsilon}}. \quad (42)$$

It can be seen from Equations 41 and 42 that the overall stress–strain relationship takes into account the corresponding responses of material both inside and outside FPZ. A length-scale parameter  $H$  is also embedded in the final formulation and hence gives the model capability in capturing the size-dependent behaviour of rocks at the constitutive level. Moreover, the double-scale model has great feasibility in incorporating any cohesive fracture law for material inside FPZ. Example for one of these models will be introduced next.

### 3.2 | Mixed-mode cohesive fracture law

A mixed-mode cohesive fracture law coupling damage mechanics and plasticity theory is employed in this study to describe the behaviour of rock material inside FPZ. The cohesive law relates the tractions ( $\mathbf{t}_c$ ) and the corresponding displacement jumps ( $\mathbf{u}_c$ ) across two faces of FPZ. For notational simplicity, subscript  $c$  is reserved in this study for all variables in the local coordinate system, representing the local behaviour of material inside FPZ, whereas subscripts  $n$  and  $s$  denote normal and shear directions, respectively. The incremental displacement jump ( $d\mathbf{u}_c$ ) can be partitioned into elastic ( $d\mathbf{u}_c^e$ ) and inelastic ( $d\mathbf{u}_c^p$ ) parts, standing for reversible and irreversible displacements, respectively:

$$d\mathbf{u}_c = d\mathbf{u}_c^e + d\mathbf{u}_c^p. \quad (43)$$

The traction state of material in FPZ can be calculated by the elastic displacement jump as

$$d\mathbf{t}_c = \mathbf{P} \mathbf{K}_{c0}^s d\mathbf{u}_c^e. \quad (44)$$

with

$$\mathbf{K}_{c0}^s = \begin{bmatrix} K_n & 0 \\ 0 & K_s \end{bmatrix} \quad (45)$$

$$\mathbf{P} = \begin{cases} \begin{bmatrix} 1-D & 0 \\ 0 & 1-D \end{bmatrix} & \text{when } t_{c(n)} \geq 0 \\ \begin{bmatrix} 1 & 0 \\ 0 & 1-D \end{bmatrix} & \text{when } t_{c(n)} < 0 \end{cases}, \quad (46)$$

where  $\mathbf{K}_c^s = \mathbf{P} \mathbf{K}_{c0}^s$  is the secant stiffness matrix of the cohesive fracture zone;  $\mathbf{K}_{c0}^s$  denotes the elastic secant stiffness matrix of cohesive fracture zone;  $\mathbf{P}$  is a parameter matrix with respect to normal traction  $t_{c(n)}$ . The inclusion of  $\mathbf{P}$  allows the cohesive model accounting for different effects of damage on the tractions under compression and tensional conditions.  $D$  is the damage variable characterising the degradation of material strength due to fracture. When  $D$  is zero, the material is elastic, but the material is fully damaged when  $D$  is approaching to unit. Thus, the evolution of damage variable  $D$  is expressed as an exponential function of the accumulated inelastic displacement jump written as<sup>32</sup>

$$D = \max\left(D_{\text{pre}}, 1 - e^{-\left(\frac{u_n^p}{\delta_0} + \frac{u_s^p}{\delta_0}\right)}\right), \quad (47)$$

where  $D_{\text{pre}}$  is the damage variable in the previous step,  $\delta_0$  is the displacement jump corresponding to the peak normal traction,  $u_n^p$  and  $u_s^p$  are respectively normal and shear inelastic displacement jumps which will be introduced later. Unlike the linear softening law described in our previous work<sup>72</sup> in which the damage variable is calculated only based on the degraded tensile strength, the incorporation of both normal and shear inelastic displacement jumps into the evolution of damage variable gives the model capability in capturing material failure under both tensile and shear loading.

Provided that the traction–displacement jump relationship and the evolution of damage variable are determined, a failure function is required to cater for the combined influence of normal and shear tractions. To be specific, the failure function is employed to determine whether material is within elastic or plastic-damage regimes and then to compute the current traction states depending on different cases. In this study, a modified form of the Mohr–Coulomb failure criterion is adopted to represent failure states expressed as

$$f(t_n, t_s, D) = t_s^2 - 2c_0(1-D)\tan\phi(\sigma_{t0}(1-D) - t_n) - \tan^2\phi(t_n^2 - (\sigma_{t0}(1-D))^2), \quad (48)$$

where  $\phi$  is the friction angle of material;  $c_0$  and  $\sigma_{t0}$  represent the initial cohesion and tensile strength, which are the controlling variables for the tensile loading and shear loading respectively. Those three values are kept unchanged during the calculation process; however, the geometry of the yield function is changed with the evolution of damage variable  $D$ , as illustrated in Figure 2.

A non-associated plastic potential is also used in this study taking into account the effect of dilatancy angle, the formulation of which is written as

$$g(t_n, t_s, D) = t_s^2 - 2c_0(1-D)\tan\psi(\sigma_{t0}(1-D) - t_n) - \tan^2\psi(t_n^2 - (\sigma_{t0}(1-D))^2), \quad (49)$$

where  $\psi$  is the dilatancy angle of material. The incremental plastic displacement jump can be computed by the non-associated flow rule as

$$d\mathbf{u}_c^p = d\lambda \frac{\partial g}{\partial t_c}, \quad (50)$$

where  $d\lambda$  is the plastic multiplier, which is a non-negative and can be determined based on the current traction state and loading history.

In the above cohesive fracture model, there are a set of constitutive parameters, including an elastic secant stiffness  $\mathbf{K}_{c0}^s$  consisting of normal stiffness  $K_n$  and shear stiffness  $K_s$ , a parameter  $\delta_0$  controlling the evolution of damage and shear strength parameters such as initial tensile strength  $\sigma_{t0}$ , initial cohesion  $c_0$ , friction angle  $\phi$  and dilatancy angle  $\psi$ . The normal stiffness  $K_n$  stands for the initial elastic stiffness of material in FPZ; thus, it can be calculated by  $K_n = E/h$ , where  $h$  is the thickness of FPZ. As mentioned before, the FPZ of rock is regarded as zero thickness; thus, the value of normal elastic stiffness  $K_n$  is approaching to infinity. As a result,  $K_n$  is selected to be a few orders of magnitude larger than  $E$  for numerical simulation. The shear stiffness  $K_s$  is the elastic stiffness in the pure shear test and can be computed from the experiment. Because our model mainly focuses on rock failure under pure mode I and mixed tensile–shear loading, the shear stiffness  $K_s$  is simply selected as be the similar order of magnitude as Young's modulus  $E$ . Another key parameter to be determined is  $\delta_0$ , which controls softening behaviour in cohesive fracture model. The value of  $\delta_0$  has to be satisfied with the requirement that the area under the traction curve depicted in Figure 3 is equal to the input fracture energy, that is,  $\int_0^{u_f} t_n du_n = G_f$ . As for other material parameters ( $\sigma_{t0}$ ,  $c_0$ ,  $\phi$  and  $\psi$ ), they can be estimated from some laboratory experiments (e.g., uniaxial compression, shear and triaxial tests), and those values are directly used in our simulation tests.

### 3.3 | Stress return algorithm of cohesive fracture law

An appropriate numerical algorithm is required for correctly updating tractions from a given displacement jump. In this work, a semi-implicit stress return algorithm is adopted. Given an incremental displacement jump  $d\mathbf{u}_c$ , the predictor

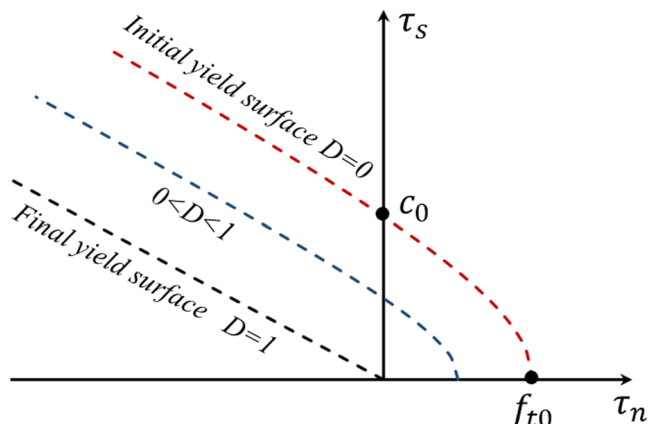


**FIGURE 2** Illustration of the shrinking of yield function against the evolution of damage variable [Colour figure can be viewed at [wileyonlinelibrary.com](http://wileyonlinelibrary.com)]

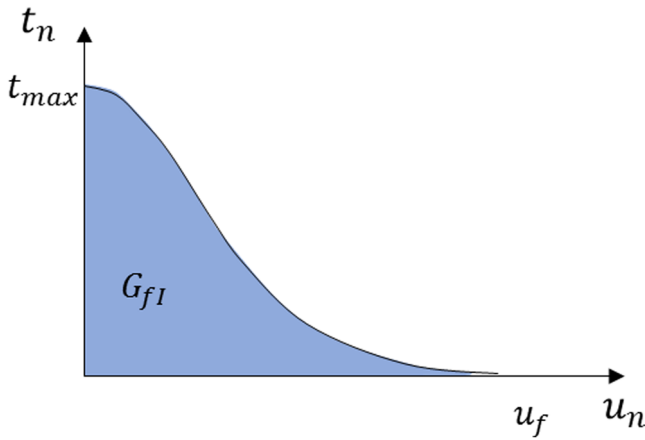


**FIGURE 3** Determination of model parameters in traction-displacement jump curves [Colour figure can be viewed at [wileyonlinelibrary.com](http://wileyonlinelibrary.com)]

traction  $\mathbf{t}_c^{\text{trial}}$  can be calculated using Equation 44. The trial yield function  $f^{\text{trial}}$  based on the elastic traction predictor is then computed by using Equation 48. If the trial yield function  $f^{\text{trial}} < 0$ , no further action is required, and the trial traction is accepted to be the correct one. In contrast, if the trial traction  $f^{\text{trial}} \geq 0$ , the correct stress can be calculated using the Taylor expansion of yield function, written as

$$f = f^{\text{trial}} + \frac{\partial f^T}{\partial \mathbf{t}_c} \frac{\partial \mathbf{t}_c}{\partial \mathbf{u}_c^p} d\mathbf{u}_c^p + \frac{\partial f^T}{\partial D} \frac{\partial \mathbf{t}_c}{\partial D} dD + \frac{\partial f}{\partial D} dD = 0, \quad (51)$$

where  $dD$  can be expressed as a function of  $d\lambda$  based on the Equations 47 and 50:

$$dD = \frac{\partial D}{\partial u_n^p} du_n^p + \frac{\partial D}{\partial u_s^p} du_s^p = d\lambda \left( \frac{\partial D}{\partial u_n^p} \frac{\partial g}{\partial t_n} + \frac{\partial D}{\partial u_s^p} \frac{\partial g}{\partial t_s} \right) = d\lambda R. \quad (52)$$

Substituting Equations 52 and 50 into Equation 51, the plastic multiplier  $d\lambda$  is calculated as

$$d\lambda = \frac{-f^{\text{trial}}}{\frac{\partial f^T}{\partial \mathbf{t}_c} \frac{\partial \mathbf{t}_c}{\partial \mathbf{u}_c^p} \frac{\partial g}{\partial t_c} + \frac{\partial f^T}{\partial D} \frac{\partial \mathbf{t}_c}{\partial D} R + \frac{\partial f}{\partial D} R}. \quad (53)$$

Once  $d\lambda$  is determined, the change of damage variable  $dD$  and the increment of plastic displacement jump  $d\mathbf{u}_c^p$  can be calculated accordingly by solving Equations 52 and 50. Finally, the corrected traction is returned using the following equation:

$$\mathbf{t}_c = \mathbf{t}_c^{\text{trial}} + \frac{\partial \mathbf{t}_c}{\partial \mathbf{u}_c^p} d\mathbf{u}_c^p + \frac{\partial \mathbf{t}_c}{\partial D} dD. \quad (54)$$

The stress return algorithm of cohesive fracture law is summarised in Algorithm 1.

#### 4 | IMPLICIT ALGORITHM OF CONTINUUM CONSTITUTIVE MODEL

After the introduction of key formulations of the double-scale framework and the cohesive fracture law, the criterion for determining fracture initiation and orientation is first explained in this section. Then, an implicit algorithm for stress updating based on traction continuity condition is presented, followed by its performance at the constitutive level at the end of this section.

**Algorithm 1****Stress return algorithm of cohesive fracture law**

*Input value:  $\Delta\mathbf{u}_c^{\text{trial}}$ ; Output value:  $\Delta\mathbf{t}_c$*

1. Calculate trial local traction increment:  $\Delta\mathbf{t}_c^{\text{trial}} = \mathbf{PK}_{c0}^s \Delta\mathbf{u}_c^{\text{trial}}$
2. Calculate trial yielding surface:  $f^{\text{trial}} = (t_{s1}^{\text{trial}2} + t_{s2}^{\text{trial}2}) - 2c_0(1-D)\tan\phi(\sigma_{t0}(1-D) - t_n^{\text{trial}}) - \tan^2\phi(t_n^{\text{trial}2} - (\sigma_{t0}(1-D))^2)$
3. If  $f^{\text{trial}} < 0$  then
4.  $\Delta\mathbf{t}_c = \mathbf{t}_c^{\text{trial}}, \Delta D = 0, \Delta\mathbf{u}_c^P = 0$
5. else
6. Calculate  $\Delta\lambda: \Delta\lambda = \frac{f^{\text{trial}}}{\frac{\partial f}{\partial\mathbf{t}_c} + \frac{\partial\mathbf{t}_c}{\partial\mathbf{u}_c^P}\frac{\partial\mathbf{u}_c^P}{\partial\mathbf{t}_c} + \frac{\partial f}{\partial\mathbf{t}_c}\frac{\partial\mathbf{t}_c}{\partial D}R + \frac{\partial f}{\partial R}}$
7. Calculate increment of local plastic displacement jump  $\Delta\mathbf{u}_c^P = \Delta\lambda \frac{\partial\mathbf{g}}{\partial\mathbf{t}_c}$
8. Calculate increment of damage variable:  $\Delta D = \Delta\lambda R$
9. Calculate increment of traction:  $\Delta\mathbf{t}_c = \Delta\mathbf{t}_c^{\text{trial}} + \frac{\partial\mathbf{t}_c}{\partial\mathbf{u}_c^P} \Delta\mathbf{u}_c^P + \frac{\partial\mathbf{t}_c}{\partial D} \Delta D$
10. Endif
11. Update local plastic displacement jump, damage variable  
 $D = D + \Delta D; \mathbf{u}_c^P = \mathbf{u}_c^P + \Delta\mathbf{u}_c^P$

**4.1 | Fracture initiation and its orientation**

As stated in Section 3, the material is initially treated as homogenous and elastic until the local fracture is triggered, after which the response of the material bifurcates into two different branches for material inside and outside FPZ, respectively. Therefore, an important question now is how to detect the correct onset of fracture and also determine the associated orientation of the fracture plane. In this study, a scanning technique is used in which the local tractions of all possible fracture orientations  $\mathbf{n}$  varying from  $0^\circ$  to  $180^\circ$  are calculated as follows:

$$\mathbf{t}_c = \mathbf{R}\mathbf{n}^T \boldsymbol{\sigma}. \quad (55)$$

Then, the yield function value  $f(t_n, t_s, D)$  corresponding to each traction is calculated. Fracture initiates when a traction state  $(t_n^*, t_s^*)$  at any rotational plane gives the maximum positive yield function  $f(t_n^*, t_s^*, D)$  in Equation 48. Once the fracture is triggered, scanning is stopped, and the fracture orientation is saved for the rest of calculation.

**4.2 | Implicit stress return algorithm for the traction continuity condition**

Beyond the onset of fracture, the homogeneity of material is lost, and the responses of material inside and outside PFZ on the given strain increment will be different. Those two responses are coupled via the traction continuity across the boundaries of FPZ as formulated in Equation 40. Thus, a stress return mapping algorithm is required for the constitutive model to track the evolution of two distinct material responses, with the traction continuity condition guaranteed at the same time. In this study, the implicit algorithm proposed by Nguyen et al.<sup>92</sup> is adopted, which starts with the calculation of elastic displacement jump increment  $d\mathbf{u}_c^{\text{trial}}$  from the input of strain increment  $d\epsilon$  based on an assumption that the material is under elastic behaviour

$$d\mathbf{u}_c^{\text{trial}} = \left( \frac{1}{H} \mathbf{n}^T \mathbf{a}_0 \mathbf{n} + \mathbf{R}^T \mathbf{K}_c^s \mathbf{R} \right)^{-1} \mathbf{n}^T \mathbf{a}_0 d\epsilon. \quad (56)$$

The trial macro-stress  $\boldsymbol{\sigma}^{\text{trial}}$  and trial local traction  $\mathbf{t}_c^{\text{trial}}$  can be then calculated from  $d\mathbf{u}_c^{\text{trial}}$  by using Equations 41 and 55, respectively. The local trial traction  $\mathbf{t}_c^{\text{trial}}$  is afterwards substituted back to the yield function  $f^{\text{trial}}$  as formulated in Equation 48. If  $f^{\text{trial}} < 0$ , the assumption of elasticity is correct, and all variables at the new state are updated elastically.

On the contrary, the material is under inelastic loading, and the stress return algorithm in Section 3.3 needs to be applied for calculating the corrected traction vectors  $\mathbf{t}_c$ . In that case, the traction continuity in Equation 40,  $\mathbf{n}^T \boldsymbol{\sigma} - \mathbf{t}_{in} = \mathbf{0}$  where  $\mathbf{t}_{in} = \mathbf{R}^T \mathbf{t}_c$  is not met; thus, an iteration process is required to satisfy the condition, which starts with the calculation of traction residual across FPZ as

$$\mathbf{r} = \mathbf{n}^T \boldsymbol{\sigma} - \mathbf{t}_{in}. \quad (57)$$

Thus, the first order Taylor expansion at the new state in terms of traction residual can be expressed as

$$\mathbf{r}^{new} = \mathbf{r}^{old} + \mathbf{n}^T \delta \boldsymbol{\sigma} - \delta \mathbf{t}_{in} = \mathbf{r}^{old} - \frac{1}{H} \mathbf{n}^T \mathbf{a}_0 \mathbf{n} \delta \mathbf{u} - \mathbf{K}^t \delta \mathbf{u}, \quad (58)$$

where  $\delta \boldsymbol{\sigma}$  and  $\delta \mathbf{t}_{in}$  are the iterative macro-stress and the iterative inside traction in global coordinate at the new state, which are calculated by the following equations:

$$\delta \boldsymbol{\sigma} = -\frac{1}{H} \mathbf{n}^T \mathbf{a}_0 \mathbf{n} \delta \mathbf{u}, \quad (59)$$

$$\delta \mathbf{t}_{in} = \mathbf{K}^t \delta \mathbf{u}, \quad (60)$$

where  $\mathbf{K}^t$  is the tangent stiffness of cohesive fracture law, which will be introduced in the next section. It should be noted here that the iterative strain  $\delta \epsilon$  is neglected in Equation 59 as it has been considered during the calculation of trial stress before performing the iteration process. By enforcing the requirement  $\mathbf{r}^{new} = \mathbf{0}$  and combining Equations 58–60, the iterative displacement jump  $\delta \mathbf{u}$  can be solved as

$$\delta \mathbf{u} = \left( \frac{1}{H} \mathbf{R} \mathbf{n}^T \mathbf{a}_0 \mathbf{n} + \mathbf{R}^T \mathbf{K}_c^t \mathbf{R} \right)^{-1} \mathbf{r}^{old}. \quad (61)$$

Once  $\delta \mathbf{u}$  has been computed, the iterative stress can be calculated based on Equation 59. In the meantime, the iterative traction in the local coordinate  $\delta \mathbf{t}_c$  can be obtained from  $\delta \mathbf{u}_c$  following a stress return algorithm (Algorithm 1). The iteration process described above will keep repeating until traction residual  $\mathbf{r}$  meets the following convergence criterion:

$$\frac{\|\mathbf{r}^{old}\|}{\|\mathbf{n}^T \boldsymbol{\sigma}_0\|} \leq \text{TOLERANCE}, \quad (62)$$

where TOLERANCE is a very small value and set as  $10^{-4}$  in this study.

### 4.3 | Calculation of tangent stiffness of cohesive fracture law

To complete the implicit algorithm, the tangent stiffness  $\mathbf{K}_c^t$  of cohesive fracture law appearing in Equation 61 needs to be calculated explicitly for each iteration step. It can be achieved by using the consistency condition with respect to yield function  $f$ :

$$df = \frac{\partial f}{\partial \mathbf{t}_c} d\mathbf{t}_c + \frac{\partial f}{\partial D} dD = 0. \quad (63)$$

As the local traction  $\mathbf{t}_c$  is a function of displacement jump, plastic displacement jump and damage variable, the incremental form of local traction can be expressed as

$$d\mathbf{t}_c = \frac{\partial \mathbf{t}_c}{\partial \mathbf{u}_c} d\mathbf{u}_c + \frac{\partial \mathbf{t}_c}{\partial \mathbf{u}_c^p} d\mathbf{u}_c^p + \frac{\partial \mathbf{t}_c}{\partial D} dD. \quad (64)$$

Substituting Equations 50, 52 and 64 into Equation 63 and solving the obtained equation for  $d\lambda$  lead to

$$d\lambda = \frac{-\frac{\partial f}{\partial \mathbf{t}_c} \frac{\partial \mathbf{t}_c}{\partial \mathbf{u}_c}}{\frac{\partial f}{\partial \mathbf{t}_c} \frac{\partial g}{\partial \mathbf{u}_c} + \frac{\partial f}{\partial \mathbf{t}_c} \frac{\partial g}{\partial D} R + \frac{\partial y}{\partial D} R} d\mathbf{u}_c = \mathbf{M} d\mathbf{u}_c, \quad (65)$$

where  $\mathbf{M}$  is a one by three matrix.

By combining Equations 64 and 65, the increment of local traction can be written as

$$d\mathbf{t}_c = \left( \frac{\partial \mathbf{t}_c}{\partial \mathbf{u}_c} + \frac{\partial \mathbf{t}_c}{\partial \mathbf{u}_c^p} \frac{\partial g}{\partial \mathbf{t}_c} \mathbf{M} + R \mathbf{M} \right) d\mathbf{u}_c, \quad (66)$$

where the tangent stiffness  $\mathbf{K}_c^t$  of cohesive fracture law in the loading case is formulated as

$$\mathbf{K}_c^t = \frac{\partial \mathbf{t}_c}{\partial \mathbf{u}_c} + \frac{\partial \mathbf{t}_c}{\partial \mathbf{u}_c^p} \frac{\partial g}{\partial \mathbf{t}_c} \mathbf{M} + R \frac{\partial \mathbf{t}_c}{\partial D} \mathbf{M}. \quad (67)$$

#### 4.4 | Summary of the implicit algorithm of the constitutive model

This section presents the summary of the implicit algorithm for stress update and all other internal variables, from the input of strain increment shown as Algorithm 2. This implicit algorithm includes all the loading scenarios from the elastic stage to final failure stage.

#### 4.5 | Behaviour of the constitutive model

After introducing the algorithm of the double-scale constitutive model with an embedded mixed-mode cohesive FPZ, an element test under complex loading conditions is carried out to illustrate the constitutive response of the model. In this test, a RVE with a length of 4 mm made from a soft rock so-called Johnstone is employed. The mechanical properties of this rock are taken from the experiment of Lim et al.<sup>6</sup> and listed in Table 1. Four different loading conditions are applied to the RVE for examining model behaviour at different loading stages, which includes (1) loading under pure mode I, (2) loading under mixed mode and (3) unloading and (4) reloading under mixed-mode condition, as illustrated in Figure 4. In the first loading stage, a constant strain increment  $\Delta \epsilon_{xx} = 3 \times 10^{-7}$  in the horizontal direction is applied to the element. During this stage, the fracture is initiated and the element has experienced the softening behaviour. In the second loading stage, the element undergoes mixed-mode loading, which is achieved by adding a constant shear strain increment  $\Delta \epsilon_{xy} = 15 \times 10^{-7}$  to the element. The behaviour of the element under unloading and reloading conditions are examined in Stage 3 and Stage 4, respectively.

The responses of the constitutive model with mixed-mode cohesive fracture law are demonstrated in Figure 5. In this figure, the model behaviour at the macroscopic level is illustrated by the stress-strain relationships in  $xx$  and  $xy$  directions (Figure 5A,B), whereas the local traction-displacement jump relationships in the normal and shear directions represent the corresponding responses of material in FPZ under different loading conditions (Figure 5C,D). At the beginning of the test (i.e., Stage 1), the pure mode I behaviour of Johnstone is observed, in which  $\sigma_{xx}$  increases linearly with its corresponding strain  $\epsilon_{xx}$ . In the meanwhile, the local traction in the normal direction  $t_n$  increases without any development in the normal displacement jump. This is due to the fact that the element is under homogenous deformation without any fracture detected inside the element. The element deforms elastically until the initiation of fracture where the state of local traction reaches its yield surface. Beyond the onset of fracture, the normal traction  $t_n$  decreases with the increase of normal displacement jump  $u_n$ , which is controlled by its cohesive fracture parameters such as fracture energy and its damage evolution law. In the meanwhile,  $\sigma_{xx}$  at the macroscopic scale reduces as the tensile loading

## Algorithm 2

### Implicit algorithm of double-scale model

*Input value:  $\Delta\epsilon$ ; Output value:  $\Delta\sigma$*

1. Initial value: para = 0, D = 0;
2. Update strain for  $=N+1$ ,  $\epsilon^{N+1} = \epsilon^N + \Delta\epsilon$ ;
3. If (para = 0) then % Haven't cracked
4. Calculate elastic trial stress  $\sigma^{\text{trial}}$  for  $t = N+1$ ;
5. Scanning and finding possible fracture plane;
6. Calculate trial traction in global coordinate:  $\mathbf{t}^{\text{trial}} = \mathbf{n}^T \sigma^{\text{trial}}$ ;
7. Calculate trial traction in local coordinate:  $\mathbf{t}_c^{\text{trial}} = \mathbf{R}\mathbf{t}^{\text{trial}}$ ;
8. Calculate maximum failure function:  $f_{\max} = (t_{s1}^{\text{trial}2} + t_{s2}^{\text{trial}2}) - 2c_0(1-D)\tan\phi(\sigma_{t0}(1-D) - t_n^{\text{trial}}) - \tan^2\phi(t_n^{\text{trial}2} - (\sigma_{t0}(1-D))^2)$
9. If ( $f_{\max} < 0$ ) then
10. Update stress and all the internal variables:  $D^{N+1} = D^N$ ,  $\sigma^{N+1} = \sigma^{\text{trial}}$
11. Elseif ( $f_{\max} \geq 0$ ) then % first crack
12. Para = 1
13. Record normal vector  $\mathbf{n}$  and rotation matrix  $\mathbf{R}$
14. Go to line 17
15. Endif
16. Elseif (para = 1) then % Already cracked
17. Calculate increment of trial displacement jump in global coordinate:  

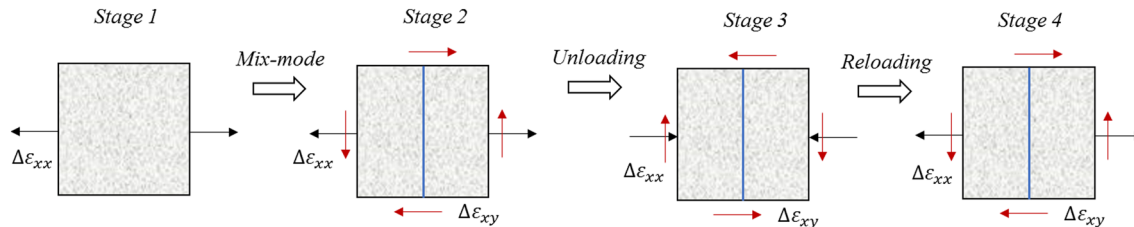
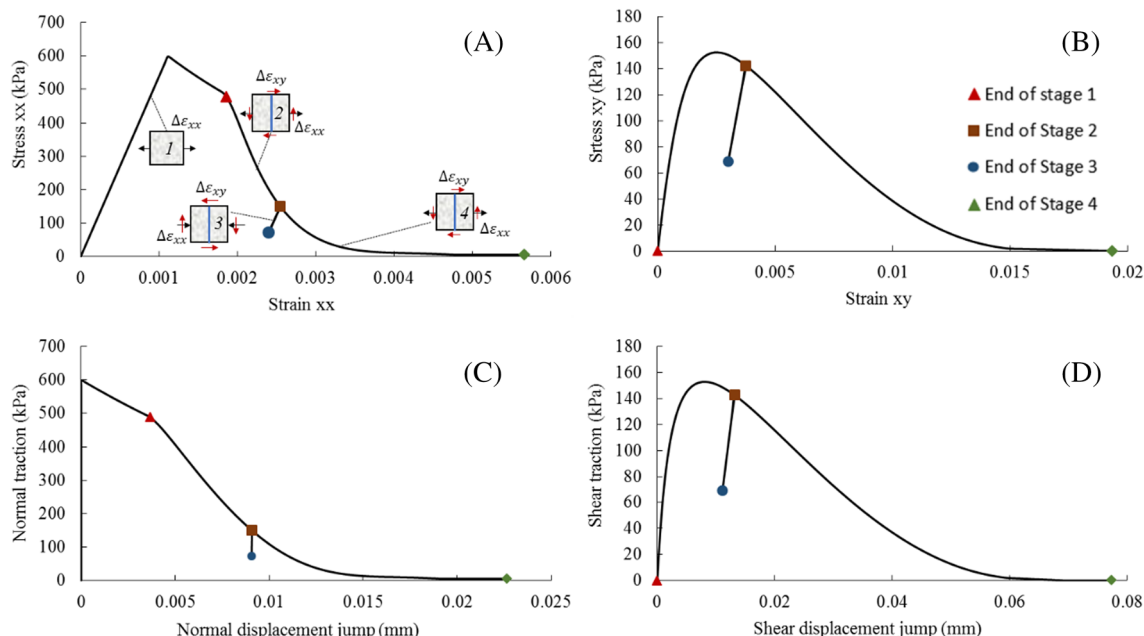
$$\Delta\mathbf{u}^{\text{trial}} = \left(\frac{1}{H}\mathbf{n}^T \mathbf{a}_0 \mathbf{n} + \mathbf{R}^T \mathbf{K}_c^{\text{trial}} \mathbf{R}\right)^{-1} \mathbf{n}^T \mathbf{a}_0 \Delta\epsilon = \mathbf{C}^{-1} \mathbf{n}^T \mathbf{a}_0 \Delta\epsilon$$
18. Calculate increment of displacement jump in local coordinate:  $\Delta\mathbf{u}_c^{\text{trial}} = \mathbf{R}\Delta\mathbf{u}$
19. Calculate trial stress increment:  $\Delta\sigma = \mathbf{a}_0 : (\Delta\epsilon - \frac{1}{H}\mathbf{n}^T \Delta\mathbf{u})$
20. Update trial stress for  $t = N+1$ :  $\sigma^{\text{trial}} = \sigma^N + \Delta\sigma$
21. Calculate trial traction in local coordinate  $\mathbf{t}_c^{\text{trial}} = \mathbf{t}_c^N + \mathbf{R}\mathbf{n}^T \Delta\sigma$
22. Calculate failure function:  $f = (t_{s1}^{\text{trial}2} + t_{s2}^{\text{trial}2}) - 2c_0(1-D)\tan\phi(\sigma_{t0}(1-D) - t_n^{\text{trial}}) - \tan^2\phi(t_n^{\text{trial}2} - (\sigma_{t0}(1-D))^2)$
23. If ( $f \leq 0$ ) then % elastic unloading/reloading
24. Update stress and all the internal variables:  $D^{N+1} = D^N$ ,  $\sigma^{N+1} = \sigma^{\text{trial}}$ ,  $\mathbf{t}^{N+1} = \mathbf{t}^{\text{trial}}$ ,  $\mathbf{t}_c^{N+1} = \mathbf{t}_c^{\text{trial}}$
25. Elseif ( $f > 0$ ) then % inelastic loading
26. Calculate  $\Delta\mathbf{t}_c$  from  $\Delta\mathbf{u}_c^{\text{trial}}$  following the procedure starting step 6 in Algorithm 1;
27. Update traction  $\mathbf{t}_c = \mathbf{t}_c^N + \Delta\mathbf{t}_c$  and calculate residual  $\mathbf{r} = \mathbf{n}^T \sigma^{\text{trial}} - \mathbf{R}^T \mathbf{t}_c$ ;
28. While  $\|\mathbf{r}\| \geq \text{TOLERANCE}$
29. Calculate  $\mathbf{K}_c^t$  with the new updated internal variable;
30. Calculate residual displacement in global coordinate:  $\delta\mathbf{u} = \left(\frac{1}{H}\mathbf{n}^T \mathbf{a}_0 \mathbf{n} + \mathbf{R}^T \mathbf{K}_c^t \mathbf{R}\right)^{-1} \mathbf{r}$ ;
31. Calculate residual displacement in local coordinate:  $\delta\mathbf{u}_c = \mathbf{R}\delta\mathbf{u}$ ;
32. Calculate  $\delta\mathbf{t}_c$  from  $\delta\mathbf{u}_c$  following the procedure starting step 6 in Algorithm 1;
33. Calculate  $\delta\sigma = -\frac{1}{H}\mathbf{a}_0 \mathbf{n} \delta\mathbf{u}$ ;
34. Update  $\sigma = \sigma + \delta\sigma$ ;  $\mathbf{t}_c = \mathbf{t}_c + \delta\mathbf{t}_c$ ;  $\mathbf{u}_c = \mathbf{u}_c + \delta\mathbf{u}_c$ ;
35. Calculate residual  $\mathbf{r} = \mathbf{n}^T \sigma - \mathbf{R}^T \mathbf{t}_c$
36. Endwhile
37. Endif
38. Endif

continues, indicating a softening response from the material. Both macro-stress in  $xy$  direction  $\sigma_{xy}$  and shear traction in the local coordinate  $t_s$  remain zero owing to the pure mode I loading condition.

In the second stage where an additional strain increment  $\epsilon_{xy}$  is applied for providing a shear force on the element, the material undergoes softening behaviour under the mixed-mode loading condition. In this case, the shear traction

**TABLE 1** Material properties of Johnstone

Material properties of soft rock	
Young's modulus ( $E$ )	0.4 GPa
Poisson ratio ( $\nu$ )	0.25
Density ( $\rho$ )	1.54 g/cm <sup>3</sup>
Tensile strength( $f_t$ )	0.6 MPa
Cohesion ( $c$ )	1.0 MPa
Friction angle ( $\varphi$ )	33°
Dilation angle ( $\psi$ )	4°
Mode I fracture toughness ( $K_{Ic}$ )	2.15 MPa/ $\sqrt{\text{mm}}$
Mode II fracture toughness ( $K_{IIc}$ )	1.05 MPa/ $\sqrt{\text{mm}}$
Peak displacement ( $\delta_0$ )	18 $\mu\text{m}$
Secant normal stiffness ( $K_{n0}$ )	1. $d13$ Pa/m
Secant shear stiffness ( $K_{s0}$ )	1. $d11$ Pa/m

**FIGURE 4** Loading paths for illustration of the constitutive behaviour [Colour figure can be viewed at [wileyonlinelibrary.com](http://wileyonlinelibrary.com)]**FIGURE 5** Constitutive behaviour of constitutive model for different loading scenarios. (A) Stress-strain relationship in  $xx$  direction; (B) stress-strain relationship in  $xy$  direction; (C) traction-displacement jump relationship in normal direction; (D) traction-displacement jump relationship in shear direction [Colour figure can be viewed at [wileyonlinelibrary.com](http://wileyonlinelibrary.com)]

starts to develop with the increase of its corresponding displacement jump, while the normal traction still keeps reducing with a steeper slope. For each step, the tractions are corrected in order to locate right on the yield surface which is changed with the damage variable. As for the macro-behaviour of material, it is similar to the local behaviour of material in FPZ, suggesting that the softening behaviour of the element is mainly controlled by the material behaviour in FPZ where the fracture dissipation takes place. The constitutive responses under unloading and reloading are also tested in the third and last stages, respectively. During the unloading stage, the material both inside and outside PFZ behaves elastically. In that case, all macro-stress and local tractions are reducing with its corresponding strains and displacement jumps until the end of Stage 3. Then, those stresses and tractions are increasing linearly at the beginning of Stage 4 following the same stress path as that of the unloading stage until reaching to the point where the unloading starts. Beyond that point, the material undergoes the softening behaviour again under the mixed-mode tensile-shear loading.

## 5 | EXPERIMENTAL VALIDATION AND APPLICATION

After examining model behaviour under mixed-mode loading conditions at constitutive level, the mixed-mode constitutive model is implemented into traditional SPH framework for rock fracture applications. In this approach, one SPH particle is regarded as one RVE, and the stress evolution of each SPH particle under various loading conditions is described by the above mixed-mode constitutive law. Once the fracture is initiated, a fracture plane at arbitrary orientation is formed within the SPH particle, and the SPH starts to damage. With the increasing strain, the overall stresses for the damaged SPH particle reduce, and the connection of the damage SPH with its surrounding SPH particles will be weakened, thereby resulting in the separation of two damaged SPH particles. Finally, as many damaged SPH particles are formed, the fracture geometries in the proposed numerical framework are represented by a set of damaged SPH particles, each of which possesses its own FPZ with arbitrary orientations, and the full detachment (or separation) of the specimen is formed due to the separation of adjacent SPH particles. In this section, three validation tests are conducted, and their simulation results are compared with experimental results for examining the capability of the proposed SPH framework in simulating mixed-mode rock fractures.

### 5.1 | Three-point bending test

In the first validation, the 3-point bending test conducted by Bellego et al.<sup>93</sup> is simulated to demonstrate the mesh insensitiveness of the constitutive model. This test was also used in Wang et al.<sup>72</sup> to examine the capability of the Taylor SPH framework associated with the pure mode I constitutive model. Different from the previous work in Wang et al.<sup>72</sup> which requires an additional set of stress points and a Taylor time integration scheme to stabilise the numerical solution, this paper employs the conventional SPH with the standard leap-frog time integration scheme to resimulate this test. Figure 6 shows the geometry and boundary conditions of the specimen and the corresponding setup in SPH model. The dimensions of the notched beam are as follows: width  $W = 80$  mm, length  $L = 320$  mm, thickness  $B = 40$  mm and notch length  $b = 8$  mm. The beam is supported by two steel rollers at a span of 240 mm and loaded by another steel roller located on its top mid-span. The material properties obtained from the experiment are listed in Table 2. It is noted here that the cohesion and mode II fracture energy are not specified in the experiment; thus, in this study, the cohesion ( $c$ ) is assumed to be the same as tensile strength ( $f_t$ ) and mode II fracture energy ( $G_{II}$ ) is equal to mode I fracture energy ( $G_I$ ). The typical friction angle  $\varphi = 37^\circ$  is selected from Fujita et al<sup>94</sup>, and the dilation angle  $\psi = 5^\circ$  is assumed in this test. The selection of dilation angel has little effect on the simulation result.

Aiming to exam the influence of spatial discretisation on numerical solutions, three different particle discretisation sizes ( $d_x = d_y = 4, 3$  and  $2$  mm) are used to generate the computational domain in SPH simulation. The number of SPH particles corresponding to these discretisations are 1378, 3021 and 6598, repectively. The length parameter ( $H$ ) in the constitutive model is equal to the corresponding particle discretisation size for all the tests. In the numerical simulations, three-layer boundary particles are generated to impose boundary conditions as shown in Figure 6B. The boundary particles have the same discretisation size and density as the real particles. To simulate the point loading at the top mid-span in the experiment, a vertical velocity is applied on the top boundary particles. A downward velocity of 1 mm/s with ramp loading is adopted in this example as same as the 3-point bending test conducted by Wang et al,<sup>72</sup> in which the dynamic effect due to loading has been investigated and it showed that the quasi-static condition can be

**FIGURE 6** Geometry and boundary condition of 3-point bending test: (A) experimental setup and (B) smoothed particle hydrodynamics simulation setup [Colour figure can be viewed at wileyonlinelibrary.com]

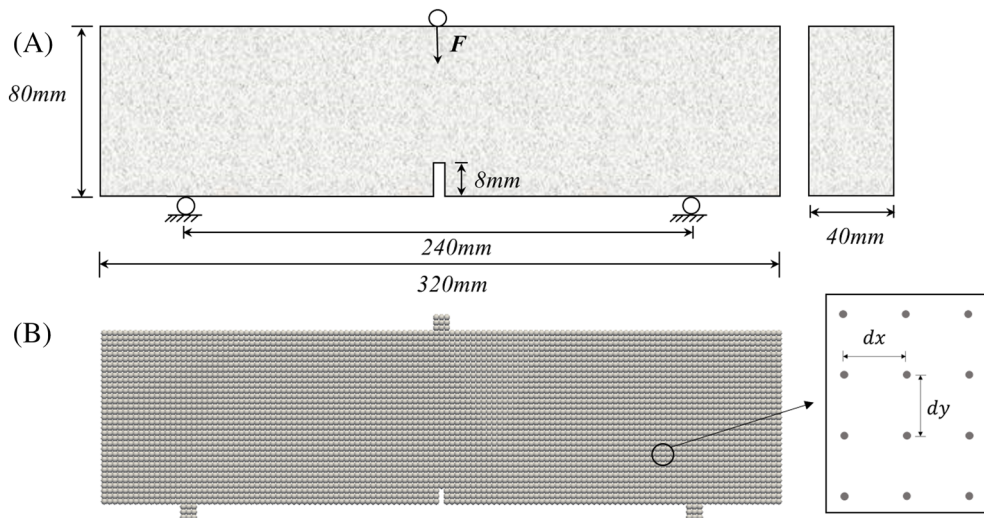


**TABLE 2** Material properties of the 3-point bending test

Material properties	
Young's modulus ( $E$ )	45 GPa
Poisson ratio ( $\nu$ )	0.24
Density ( $\rho$ )	$2.4 \frac{\text{g}}{\text{cm}^3}$
Tensile strength( $f_t$ )	2.9 MPa
Cohesion ( $c$ )	2.9 MPa
Friction angle ( $\varphi$ )	$37^\circ$
Dilation angle ( $\psi$ )	$5^\circ$
Mode I fracture energy ( $G_I$ )	47.17 Nm
Mode II fracture energy ( $G_{II}$ )	47.17 Nm
Peak displacement ( $\delta_0$ )	16.4 $\mu\text{m}$
Secant normal stiffness ( $K_{n0}$ )	$10^{14} \frac{\text{Pa}}{\text{m}}$
Secant shear stiffness ( $K_{s0}$ )	$10^{11} \frac{\text{Pa}}{\text{m}}$

achieved by using above velocity. Therefore, velocities of top boundary particles are set as  $v_x = 0, v_y = -1 \text{ mm/s}$ . On the other hand, the vertical motion of the bottom boundary particles is fixed, but it allows free moving in the horizontal direction, so  $v_y = 0$ . The stresses of all boundary particles are updated in the same way as the real particles that form the computational domain of the beam; however, the boundary particles always keep elastic. The compression stress and vertical displacement of real particles near the loading particles are recorded during the simulation process and subsequently being used for comparison with the experimental data and the simulation result of Wang et al.<sup>72</sup> using the pure mode I constitutive model.

Figure 7 shows a comparison between the experiment and the SPH simulation including pure mode I and mixed-mode constitutive model for the compressive force–deflection curve. It can be seen that the SPH model with the embedded mixed-mode cohesive fracture law can capture the overall response of the force–deflection curve in the experiment. The force initially undergoes a linear behaviour until the fracture is initiated (i.e., from  $i$  to  $h$  in Figure 7). This is then followed by the hardening response up to the peaking load (i.e., from  $h$  to  $a$  in Figure 7). Subsequently, the model experiences a softening behaviour where the stress is reduced with the increasing deflection as shown in Figure 7, *a*–*d*). The corresponding fracture patterns of (*a*) to (*d*) are illustrated in Figure 8. Figure 8A shows the fracture propagation when the compression force reaches its peak marked in Figure 7, *a*. At this point, the damage has been propagating to around half of the beam height, which is consistent with the description in the work of Wang et al.<sup>72</sup> Then, the fracture keeps propagating towards to the loading point shown in Figure 8B–D, resulting in a continuous through-running fracture

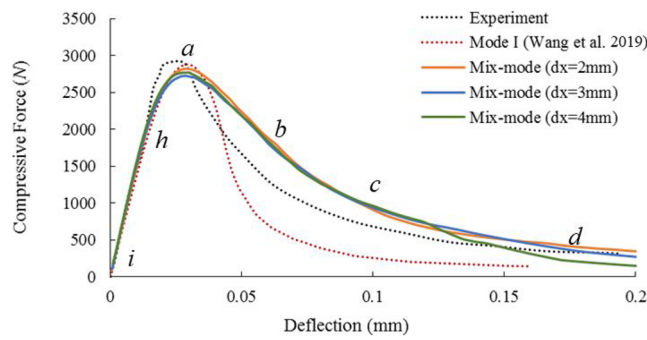


**FIGURE 7** Compressive force and deflection relationship of the 3-point bending test [Colour figure can be viewed at [wileyonlinelibrary.com](http://wileyonlinelibrary.com)]

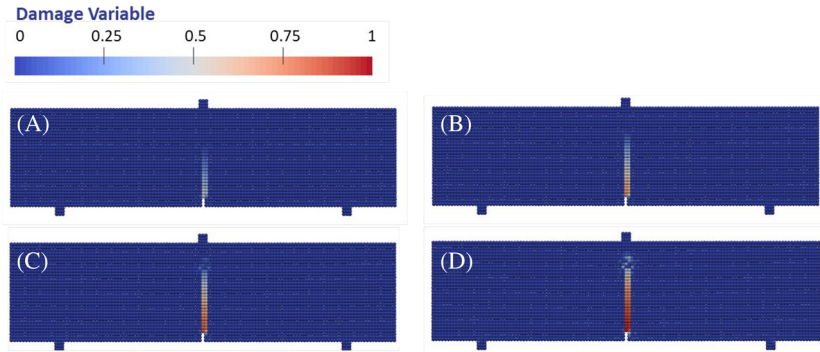


**FIGURE 8** Fracture propagation and its final pattern in the 3-point bending test [Colour figure can be viewed at [wileyonlinelibrary.com](http://wileyonlinelibrary.com)]

pattern in the middle of the beam. During the stage of both hardening and softening, the specimen experiences its fracture initiation, propagation and finally damage, which is the consequence of the progressive damage of the material in the cohesive fracture zone of each damaged SPH particle. The model response using the mixed-mode cohesive fracture law is also compared with the behaviour using the double-scale model with the embedded mode I cohesive fracture law in Taylor SPH,<sup>72</sup> as shown in Figure 7. A more ductile behaviour can be observed in the result of current model as the shear component of the cohesive fracture included in the mixed-mode model gives itself a more realistic response in capturing the correct fracture energy resistance. The results of the force–deflection curve using three different particle discretisation sizes are also plotted in Figure 7. It can be seen that the numerical results are quite similar among three cases, although there exist some minor differences. This suggests that the numerical approach is less sensitive to the spatial discretisation (or initial space between two consecutive particles).

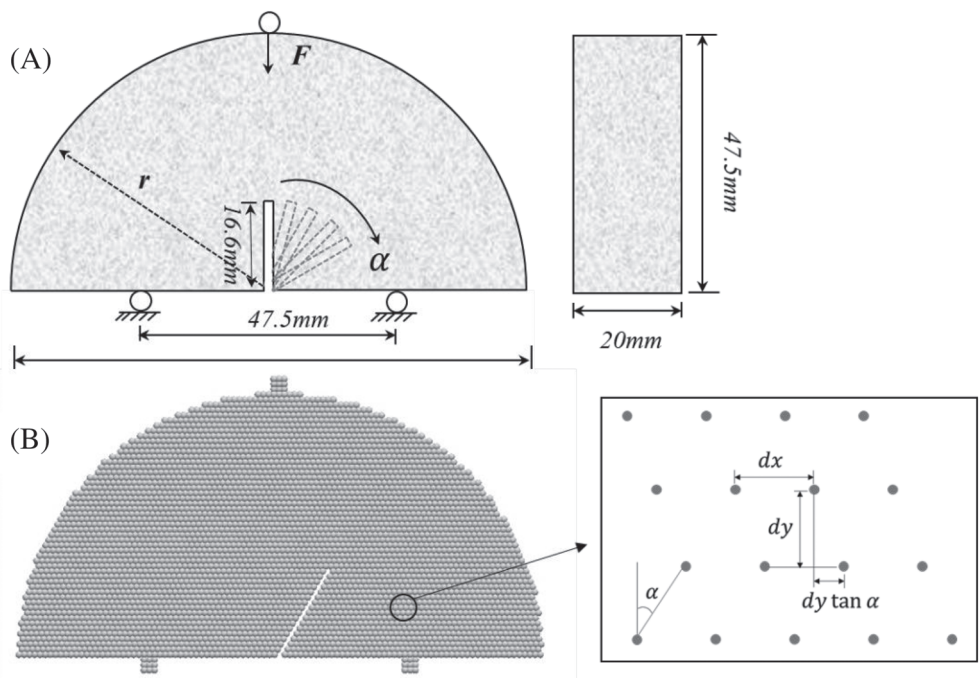
## 5.2 | Semicircular bending test

The second application to be considered is a series of semicircular bending tests on Johnstone, which have been carried out by Lim et al.<sup>95</sup> The aim of this example is to examine its predictive capability of the SPH model under a wide range of mixed-mode loading conditions. The geometry and boundary conditions of the test in the experiment are shown in Figure 9A. Similar with 3-point bending test, the semicircular specimens with a radius of 47.5 mm and a thickness of 20 mm are supported by two rollers at a span of 47.5 mm and loaded by another roller on its mid-span. Notches with a length of 16.6 mm are created with different notch angles varying from 0° to 60° with respect to the vertical axis to investigate the influences of the notch angles on the peak load ( $P$ ) and the fracture toughness ( $K_I, K_{II}$ ), which are calculated as follows:

$$K_I = \frac{P}{2rt} \sqrt{\pi a Y_I}, \quad (68)$$

$$K_{II} = \frac{P}{2rt} \sqrt{\pi a Y_{II}}, \quad (69)$$

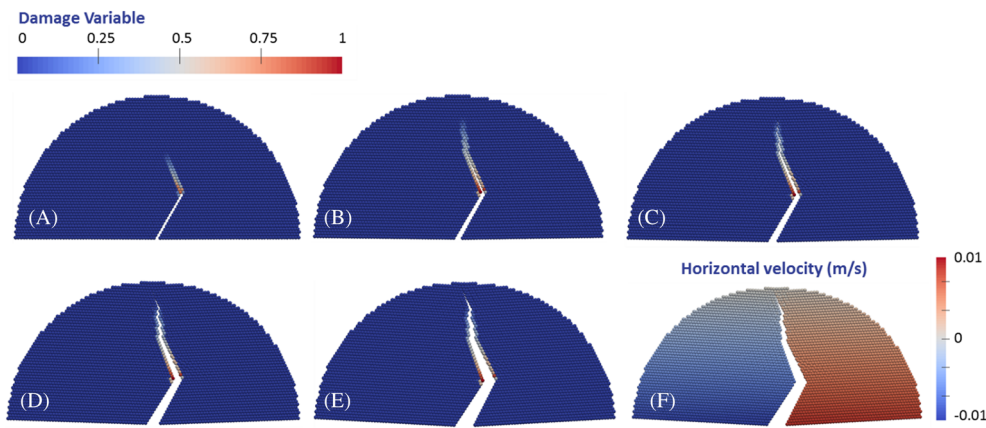
**FIGURE 9** Geometry and boundary condition of the semicircular bending test:  
(A) experimental setup and  
(B) smoothed particle hydrodynamics simulation setup when rotational angle = 30°



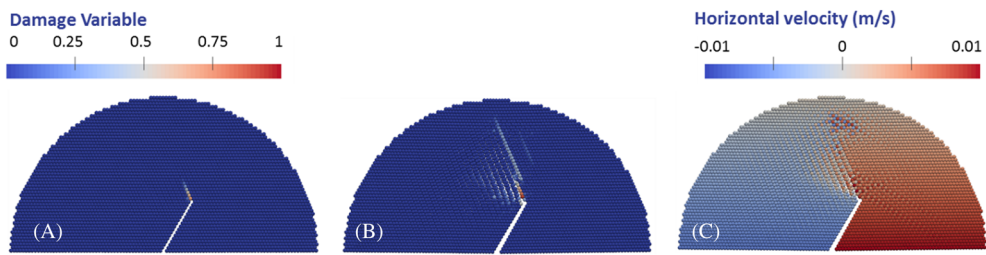
where  $K_I$  and  $K_{II}$  are respectively mode I and mode II fracture toughness;  $r$  is the specimen radius;  $t$  is the specimen thickness;  $a$  is the notch length;  $Y_I$  and  $Y_{II}$  are mode I and mode II normalised stress intensity factor. As the values of  $Y_I$  and  $Y_{II}$  can be obtained from the data by Lim et al.<sup>6</sup>  $K_I$  and  $K_{II}$  can be calculated based on the above equation once the peak load ( $P$ ) is known. The material properties of Johnstone are listed in Table 1. The friction angle and dilation angle are respectively taken as 33° and 4° for average quality rock masses in Hoek and Brown<sup>96</sup> for the following examples.

Figure 9 shows the corresponding SPH configuration of the semicircular bending test with a notch angle of 30°. In the tests, a particle discretisation of 0.95 mm is used, resulting in a total number of 3995 SPH particles for generating the specimen. To create accurate notch angles using reasonable particle numbers, the initial SPH arrangement in this test is different from the traditional one such as the 3-point bending test in Section 5.1. The initial location of each SPH particle in semicircular bending tests is related to the notch angle as shown in Figure 9B. Similar to the 3-point bending tests, three layers of boundary particles are generated for simulating the point loading in the experiments. The velocities of the top boundary particles are  $v_x = 0, v_y = -2$  mm/s, whereas the velocities of the bottom boundary particles are as  $v_y = 0$ . As Johnstone rocks are classified as soft rocks with a relatively small elastic Young's modulus, both artificial viscosity and artificial stress are used in this test to stabilise the numerical solutions. The ramp loading is also applied to alleviate the dynamic effect due to the sudden loading. The stresses of boundary particles are updated in the same way as that in the 3-point bending test. The stresses of real particles near the loading particles are recorded during the simulation process, from which the peak load and fracture toughness can be obtained for the comparison with the experimental data.

Figure 10 illustrates the progressive development of fracture and the horizontal velocity profile at the failure stage for the semicircular specimen with the rotational angle of 30°. As seen in Figure 10A, some particles near the tip of the notch are first damaged, showing that the fracture is initiated at the location of the notch tip. Then, the fracture propagates towards the loading point (Figure 10B–D), and eventually, a vertical curvilinear fracture pattern is formed in the middle of the sample (Figure 10E). The horizontal velocity profile corresponding to Figure 10E is also plotted in Figure 10F. It can be seen that the particles on the left side of the fracture move to the left whereas the particles on the other side move to the right direction; thus, the sample is split into two halves at the end. In this approach, SPH particle itself could not be cracked visually; however, each damaged SPH particle possesses a FPZ, and the material behaviour within the FPZ will contribute to the decrease in the overall stress state of the SPH particle, thereby resulting in the separation between two damaged SPH particles. The same test without using the artificial stress is also plotted in Figure 11. The result remains stable when the fracture is initiated (Figure 11A) but becomes unstable during the post-failure process (Figure 11B,C). Unrealistic fracture and particles clustering are observed in Figure 11B,C, which indicates the tensile instability problem is occurred in SPH. By comparing those two results, it can be concluded that the



**FIGURE 10** Fracture pattern for rotational angle = 30° in the semicircular bending test with tensile instability treatment: (A–E) fracture development and (F) horizontal velocity for final fracture pattern [Colour figure can be viewed at [wileyonlinelibrary.com](http://wileyonlinelibrary.com)]



**FIGURE 11** Numerical results for rotational angle = 30° in the semicircular bending test without tensile instability treatment: (A and B) fracture development and (C) horizontal velocity profile [Colour figure can be viewed at [wileyonlinelibrary.com](http://wileyonlinelibrary.com)]

tensile instability problem can be completely removed and good numerical stability can be achieved by just adopting this artificial stress term.

Figure 12 depicts the comparison of mixed-mode fracture envelope between experiments and SPH simulations for different notch inclination angles  $\alpha = 0^\circ, 15^\circ, 30^\circ, 45^\circ, 50^\circ$  and  $60^\circ$ . It shows that the simulation fracture patterns marked as red lines match well with the experimental results shown as black lines. The final fracture pattern is a vertical straight line when  $\alpha = 0^\circ$  (pure mode I). When  $\alpha > 0^\circ$ , the sample is subjected to mixed-mode or pure mode II loading, resulting in a curvilinear fracture paths. For all simulation cases, the fractures initiate from the notch tip and then propagate towards upper loading point, while the experiments show that a few fractures tend to initiate behind the notch tip when the notch angle is beyond  $\alpha = 50^\circ$ . Nevertheless, the simulation results still could successfully predict the overall fracture envelope in experiments and demonstrate the capability of the traditional SPH model for capturing

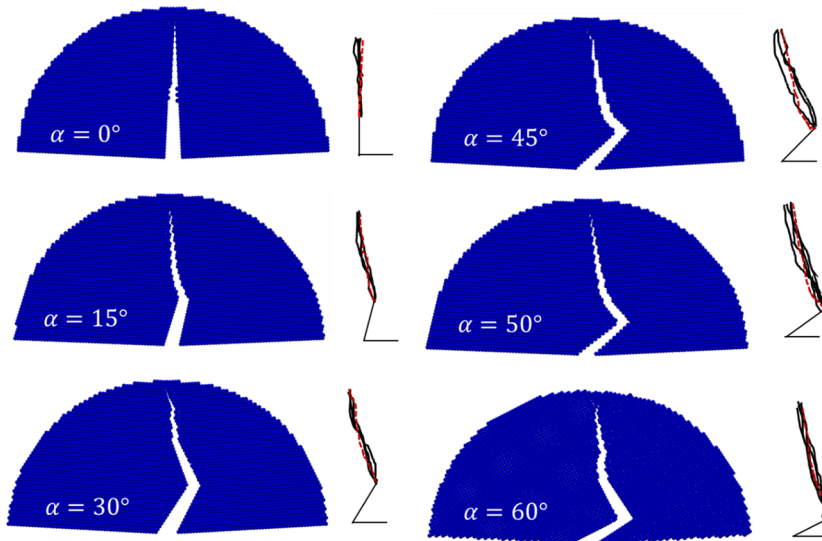


**FIGURE 12** Comparison of final fracture pattern between experimental and numerical results in the semicircular bending test [Colour figure can be viewed at [wileyonlinelibrary.com](http://wileyonlinelibrary.com)]

the fracture development under various complex loading conditions. In the meanwhile, the comparison of peak load between experiments and simulations for the notch inclination angles varying from  $0^\circ$  to  $60^\circ$  with an internal increment of  $5^\circ$  is plotted in Figure 13A. It is noted here that a notch angle of  $54^\circ$  (instead of  $55^\circ$ ) is used in the current test as the sample is subjected to pure mode II loading condition when  $\alpha = 54^\circ$ .<sup>95</sup> The SPH simulation can well capture the increasing trend of the peak load with the increasing notch angles in the experiment. Additionally, Figure 13B compares the predictions of fracture toughness in SPH simulation against the experimental results and Lim's theory.<sup>95</sup> The simulation results perfectly fall within the experimental data ranges even though the fracture toughness data in the experiments are quite scattered. Nevertheless, the numerical results agree closely with the empirical fracture toughness envelope, which was proposed by Lim et al.<sup>95</sup> and represented as a black line Figure 13B. It further confirms that our model could accurately predict the mixed-mode fracture behaviour of rocks in semicircular bending test.

**FIGURE 13** Comparison between experimental and numerical results in the semicircular bending test: (A) peak force against the notch inclination angle and (B) mode II fracture toughness against mode I fracture toughness in terms of different notch inclination angles [Colour figure can be viewed at [wileyonlinelibrary.com](http://wileyonlinelibrary.com)]

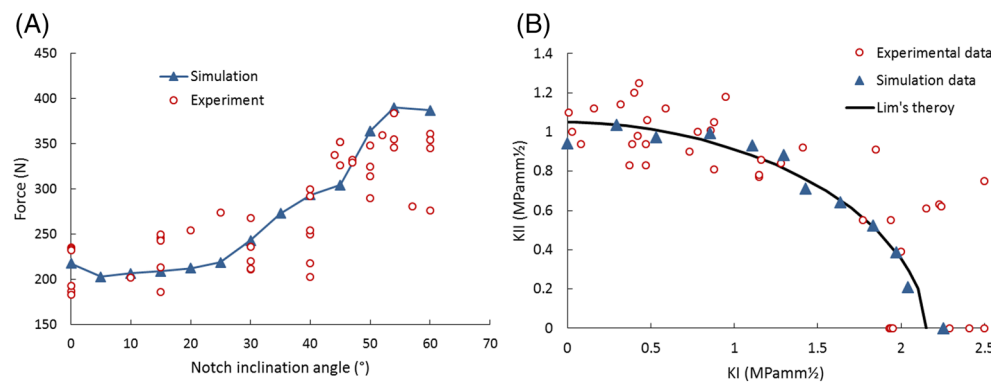


**FIGURE 14** Geometry and boundary condition of the Brazilian test: (A) experimental setup and (B) smoothed particle hydrodynamics simulation setup for  $\alpha = 0.3$

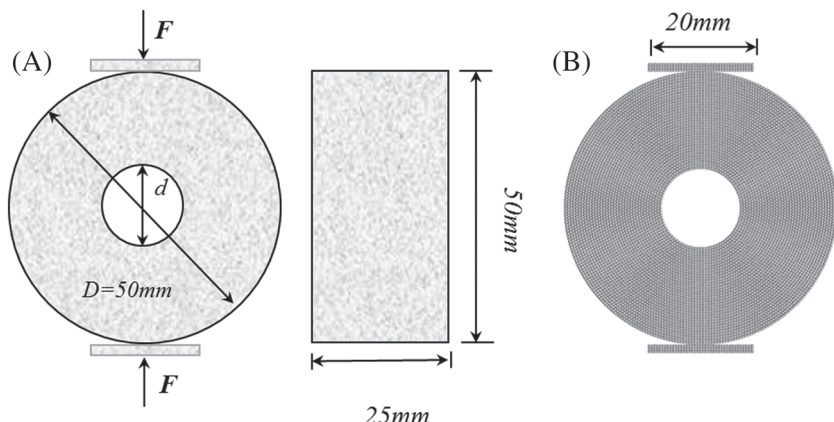


**TABLE 3** Material properties of marble in the Brazilian test

Material properties of marble	
Young's modulus ( $E$ )	49 GPa
Poisson ratio ( $\nu$ )	0.19
Density ( $\rho$ )	2.7 g/cm <sup>3</sup>
Tensile strength( $f_t$ )	3.6 MPa
Cohesion ( $c$ )	10 MPa
Friction angle ( $\varphi$ )	33°
Dilation angle ( $\psi$ )	4°
Mode I fracture energy ( $G_I$ )	30 Nm
Mode II fracture energy ( $G_{II}$ )	30 Nm
Peak displacement ( $\delta_0$ )	8.5 μm
Secant normal stiffness ( $K_{n0}$ )	$10^{14}$ Pa/m
Secant shear stiffness ( $K_{s0}$ )	$10^{11}$ Pa/m

### 5.3 | Brazilian test

To further demonstrate the predictive capability of the traditional SPH model in capturing the mixed-mode rock fracture behaviour, a series of mixed-mode Brazilian tests with different internal diameters performed by Li et al.<sup>97</sup> is simulated as the last application. The geometry and loading conditions of the specimen in the experiments are shown in Figure 14A. The specimens drilled from a marble block are firstly prepared with a diameter ( $D$ ) of 50 mm and a thickness ( $t$ ) of 25 mm. Then, a circular disc with the diameter ( $d$ ) varying from 5 to 25 mm is cut off at the centre of the specimens, resulting in the ring specimens with different diameter ratios ( $d/D$ ) from 0.1 to 0.5. Specimens are sandwiched directly between two platens, over which a static force is applied. The material properties of marble are listed in Tables 1–3. The tensile strength is obtained from the experiment by Li et al.<sup>97</sup> whereas other material properties of marble come from the work of Li et al.<sup>98</sup>

The corresponding numerical setup in SPH is shown in Figure 14B. To perfectly create the shape of circular cut-off using a reasonable number of particles, particles that form the ring sample are radial-distributed in this test. The particle discretisation size of 0.5 mm is used for all the simulations, resulting in a total number of 7651 particles for a specimen without the central hole. The particles number is decreasing with a larger value of diameter ratio ( $d/D$ ). To simulate those two platens in the experiment, three layers of boundary particles with a spatial discretisation size of 0.5 mm are generated in the traditional way as the 3-point bending test. The velocities of top boundary particles are set as  $v_x = 0, v_y = -1$  mm/s, whereas the velocities of bottom boundary particles are  $v_x = 0, v_y = 1$  mm/s.

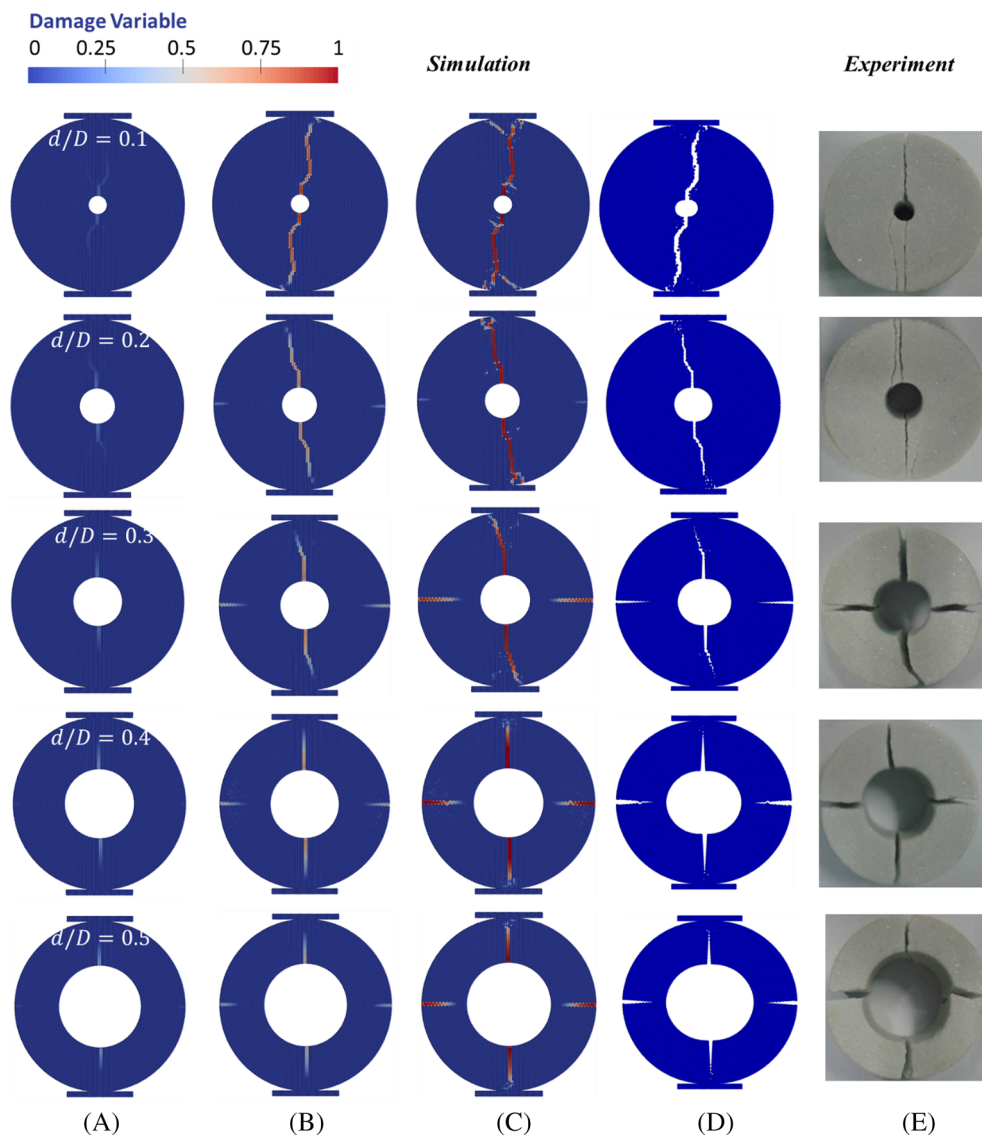
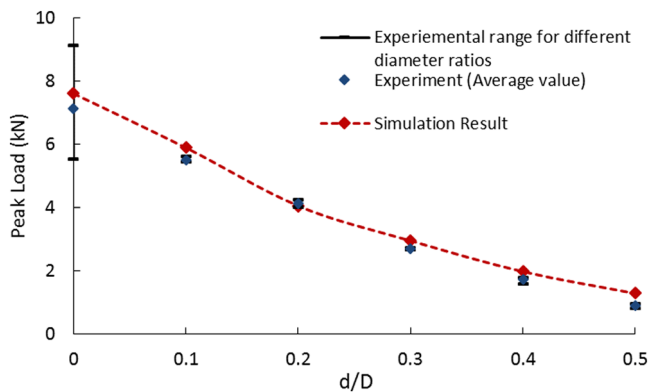


**FIGURE 15** Fracture development in smoothed particle hydrodynamics simulation and final fracture patterns of numerical and experimental results with respect to different diameter ratio ( $d/D$ ) in the Brazilian test [Colour figure can be viewed at [wileyonlinelibrary.com](http://wileyonlinelibrary.com)]

**FIGURE 16** Comparison of peak load between simulation and experimental results with respect to different ratio ( $d/D$ ) in the Brazilian test [Colour figure can be viewed at [wileyonlinelibrary.com](http://wileyonlinelibrary.com)]



The fracture development of ring specimens with different diameter ratios ( $d/D$ ) in Brazilian test is shown in Figure 15A–C. It can be seen from Figure 15 that the fracture firstly initiates from the surface of the internal hole along the diametral loading line in all ring specimens. However, specimens with different diameter ratios have different fracture envelopes. To be more specific, the fracture initiates and propagates towards the upper and lower platens, eventually forming a vertical diametrical crack along the loading line when the diameter ratio  $d/D < 0.3$ . Although some particles near the outer ring are slightly damaged when  $d/D = 0.2$ , the secondary crack has not been formed before the first crack is fully formed. With an increasing  $d/D$  ( $d/D \geq 0.3$ ), there are secondary cracks formed in the direction perpendicular to the loading line, which is always lagging behinds the vertical cracks. The secondary cracks are initiated from the surface of the outer bound of the ring and propagated to the centre, eventually resulting in four-pan-shaped failure. The final fracture patterns in SPH simulation and experiment are respectively shown in Figure 15D and Figure 15E. It can be seen that fracture pattern in the simulations matches well the fracture patterns observed in the experiments, although there exists a lightly difference in the secondary cracks when  $d/D \geq 0.3$ . In the experiment, the secondary cracks perpendicular to the loading line cut through the specimen, splitting the rock specimen into four pieces; however, the secondary cracks fail to propagate through the specimen. This indicates that the rock specimen used for the laboratory experiment is more brittle compared with the simulated specimen. The difference may be due to the inaccurate measurement of input parameters (such as fracture energy and tensile strength) in the experiment, which was directly applied in the SPH simulation. Overall, the proposed model could capture well the fracture patterns observed in the experiments, indicating that our SPH is capable of simulating multiple cracks under mixed-mode loading and predicting the progressive failure of specimens in Brazilian tests.

Figure 16 shows the comparison of peak load between SPH simulations and experiments with respect to different diameter ratios. It can be seen that our numerical model can capture well the trend of change in peak load exhibited in the experiment. When  $d/D = 0$ , which means there is no hole in the specimen, the peak load is the largest among all the cases. Although it is slightly larger than the average value of experimental results, the peak load predicted by SPH simulation is perfectly fallen within the range of experimental data when  $d/D = 0$ . With an increasing diameter ratio  $d/D$ , it shows a linearly decreasing trend in peak load. This is because the specimen with larger  $d/D$  has shorter fracture routes, thus requiring less fracture energy and a smaller peak load compared with the specimen with smaller  $d/D$ .

## 6 | CONCLUSION

A numerical approach that combines the conventional SPH method and a size-dependent constitutive model with an embedded mixed-mode cohesive fracture is presented for modelling rock fractures under both pure mode I and mixed-mode loading conditions. Through three numerical comparisons with experimental results, the following key features of the proposed numerical framework are highlighted:

- 1 The successful applications of the conventional SPH method to model progressive rock fractures confirm its simplicity, versatility and efficiency in solving complex problems, thanks to the simple tensile instability treatment technique. Compared with the Taylor SPH method in our previous work, the conventional SPH is much simpler and more robust as it does not require special treatments of free-surface boundary conditions. Thus, together with its

mesh-free nature, the conventional SPH method has a great flexibility in simulating fracture and complete detachment of rocks under various loading conditions.

- 2 The proposed constitutive model employs a mixed-mode cohesive fracture law to capture the mixed-mode fracture within the FPZ. In addition, the proposed model is able to take in account the relative size between the FPZ and the elastic surrounding bulk, leading to a length parameter embedded into the constitutive structure. The introduction of such length parameter allows modelling the cracks without suffering from any mesh dependency naturally.
- 3 The numerical approach combining the conventional SPH and the mixed-mode constitutive model is demonstrated to be able to predict the underlying failure mechanism of different types of rocks under a wide range of loading conditions. Because the fracture topology is represented by a set of damaged SPH particles, each of which possesses its own fracture plane and having arbitrary direction depending on the loading condition, the proposed numerical model is capable of capturing multiple and complex fractures.

## ACKNOWLEDGEMENTS

This work was supported by the Australian Research Council through Discovery Projects DP160100775 (Bui), FT140100408 (Nguyen), DP170103793 (Nguyen and Bui) and DP190102779 (Bui and Nguyen).

## ORCID

Ha H. Bui  <https://orcid.org/0000-0001-8071-5433>

## REFERENCES

1. Griffith AA, Eng M. VI. The phenomena of rupture and flow in solids. *Phil Trans R Soc Lond A*. 1921;221(582–593):163–198.
2. Irwin GR. Analysis of stresses and strains near the end of a crack traversing a plate. *J. appl. Mech.* 1957;24:361–364.
3. Wu CH. Fracture under combined loads by maximum-energy-release-rate criterion. *J Appl Mech.* 1978;45(3):553–558.
4. Zhang QB, Zhao J. A review of dynamic experimental techniques and mechanical behaviour of rock materials. *Rock Mech Rock Eng.* 2014;47(4):1411–1478.
5. Kuruppu MD, Chong KP. Fracture toughness testing of brittle materials using semi-circular bend (SCB) specimen. *Eng Fract Mech.* 2012;91:133–150.
6. Lim IL, Johnston IW, Choi SK. Stress intensity factors for semi-circular specimens under three-point bending. *Eng Fract Mech.* 1993;44(3):363–382.
7. Aliha MRM, Ayatollahi MR, Smith DJ, Pavier MJ. Geometry and size effects on fracture trajectory in a limestone rock under mixed mode loading. *Eng Fract Mech.* 2010;77(11):2200–2212.
8. Krishnan GR, Zhao XL, Zaman M, Roegiers JC. Fracture toughness of a soft sandstone. *Int J Rock Mech Min Sci.* 1998;35(6):695–710.
9. Choi SR, Zhu D, Miller RA. Fracture behavior under mixed-mode loading of ceramic plasma-sprayed thermal barrier coatings at ambient and elevated temperatures. *Eng Fract Mech.* 2005;72(13):2144–2158.
10. Fett T, Gerteisen G, Hahnenberger S, Martin G, Munz D. Fracture tests for ceramics under mode-I, mode-II and mixed-mode loading. *J Eur Ceram Soc.* 1995;15(4):307–312.
11. Buchholz FG, Pirro PJM., Richard HA, Dreyer KH. Numerical and experimental mixed-mode analysis of a compact tension-shear specimen. In *Numerical methods in Fracture Mechanics, Proceedings of the Fourth International Conference, San Antonio, Texas, USA* 1987; (pp. 641–656).
12. Mahajan RV, Ravi-Chandar K. An experimental investigation of mixed-mode fracture. *Int J Fract.* 1989;41(4):235–252.
13. Wells GN, Sluys LJ. Three-dimensional embedded discontinuity model for brittle fracture. *Int J Sol Struct.* 2001a;38(5):897–913.
14. De Borst R, Réthoré J, Abellán MA. A numerical approach for arbitrary cracks in a fluid-saturated medium. *Arch Applied Mech.* 2006;75(10–12):595–606.
15. Dimitri R, Fantuzzi N, Li Y, Tornabene F. Numerical computation of the crack development and SIF in composite materials with XFEM and SFEM. *Composite Struct.* 2017;160:468–490.
16. Ferté G, Massin P, Moës N. 3D crack propagation with cohesive elements in the extended finite element method. *Comput Methods Appl Mech Eng.* 2016;300:347–374.
17. Salimzadeh S, Khalili N. A three-phase XFEM model for hydraulic fracturing with cohesive crack propagation. *Comp Geotech.* 2015;69:82–92.
18. Wells GN, Sluys LJ. A new method for modelling cohesive cracks using finite elements. *Int J Numer Methods Eng.* 2001b;50(12):2667–2682.
19. Bosco E, Kouznetsova VG, Geers MGD. Multi-scale computational homogenization-localization for propagating discontinuities using XFEM. *Int J Numer Methods Eng.* 2015;102(3–4):496–527.
20. Dias-da-Costa D, Alfaiate J, Sluys LJ, Júlio ENBS. A discrete strong discontinuity approach. *Eng Fract Mech.* 2009;76(9):1176–1201.
21. Dias-da-Costa D, Alfaiate J, Sluys LJ, Júlio ENBS. A comparative study on the modelling of discontinuous fracture by means of enriched nodal and element techniques and interface elements. *Int J Fract.* 2010;161(1):97–119.

22. Dias-da-Costa D, Alfaiate J, Sluys LJ, Areias P, Júlio ENBS. An embedded formulation with conforming finite elements to capture strong discontinuities. *Int J Numer Methods Eng.* 2013;93(2):224-244.
23. Oliver J. Modelling strong discontinuities in solid mechanics via strain softening constitutive equations. Part 1: fundamentals. *Int J Numer Methods Eng.* 1996a;39(21):3575-3600.
24. Oliver J. Modelling strong discontinuities in solid mechanics via strain softening constitutive equations. Part 2: numerical simulation. *Int J Numer Methods Eng.* 1996b;39(21):3601-3623.
25. Zhang Y, Zhuang X. Cracking elements: a self-propagating strong discontinuity embedded approach for quasi-brittle fracture. *Finite Elements Anal Des.* 2018;144:84-100.
26. Borja RI. A finite element model for strain localization analysis of strongly discontinuous fields based on standard galerkin approximation. *Comput Methods Appl Mech Eng.* 2000;190(11-12):1529-1549.
27. Borja RI. Assumed enhanced strain and the extended finite element methods: a unification of concepts. *Comput Methods Appl Mech Eng.* 2008;197(33-40):2789-2803.
28. Motamedi MH, Weed DA, Foster CD. Numerical simulation of mixed mode (I and II) fracture behavior of pre-cracked rock using the strong discontinuity approach. *Int J Sol Struct.* 2016;85:44-56.
29. Reinoso J, Paggi M, Linder C. Phase field modeling of brittle fracture for enhanced assumed strain shells at large deformations: formulation and finite element implementation. *Comput Mech.* 2017;59(6):981-1001.
30. Duan K, Kwok CY, Tham LG. Micromechanical analysis of the failure process of brittle rock. *Int J Numeric Analytic Meth Geomech.* 2015;39(6):618-634.
31. Nguyen CT, Nguyen GD, Das A, Bui HH. Constitutive modelling of progressive localised failure in porous sandstones under shearing at high confining pressures. *Int J Rock Mech Min Sci.* 2017a;93:179-195.
32. Nguyen NH, Bui HH, Nguyen GD, Kodikara J. A cohesive damage-plasticity model for DEM and its application for numerical investigation of soft rock fracture properties. *Int J Plasticity.* 2017c;98:175-196.
33. Nguyen NH, Bui HH, Kodikara J, Arooran S, Darve F. A discrete element modelling approach for fatigue damage growth in cemented materials. *Int J Plasticity.* 2019;112:68-88.
34. Potyondy DO, Cundall PA. A bonded-particle model for rock. *Int J Rock Mech Min Sci.* 2004;41(8):1329-1364.
35. Rojek J, Onate E, Labra C, Kargl H. Discrete element simulation of rock cutting. *Int J Rock Mech Min Sci.* 2011;48(6):996-1010.
36. Gingold RA, Monaghan JJ. Smoothed particle hydrodynamics: theory and application to non-spherical stars. *Monthly Notices Royal Astro Soc.* 1977;181(3):375-389.
37. Lucy LB. A numerical approach to the testing of the fission hypothesis. *Astronomic J.* 1977;82:1013-1024.
38. Bui HH. Lagrangian mesh-free particle method (SPH) for large deformation and post-failure of geomaterial using elasto-plastic constitutive models. Doctoral dissertation. Ritsumeikan University. 2007.
39. Bui HH, Fukagawa R, Sako K, Ohno S. Lagrangian meshfree particles method (SPH) for large deformation and failure flows of geomaterial using elastic-plastic soil constitutive model. *Int J Numeric Analytic Meth Geomech.* 2008a;32(12):1537-1570.
40. Zhao S, Bui HH, Lemiale V, Nguyen GD. SPH simulation of strain localisation in geomaterials using a visco-plastic constitutive model. *Poromechanics VI.* 2017;1876-1883.
41. Bui HH, Fukagawa R, Sako K, Wells J. Slope stability analysis and discontinuous slope failure simulation by elasto-plastic smoothed particle hydrodynamics (SPH). *Geotechnique.* 2011;61(7):565-574.
42. Bui HH, Fukagawa R. An improved SPH method for saturated soils and its application to investigate the mechanisms of embankment failure: case of hydrostatic pore-water pressure. *Int J Numeric Analytic Meth Geomech.* 2013;37(1):31-50.
43. Peng C, Guo X, Wu W, Wang Y. Unified modelling of granular media with smoothed particle hydrodynamics. *Acta Geotechnica.* 2016; 11(6):1231-1247.
44. Bui HH, Nguyen GD. Numerical predictions of post-flow behaviour of granular materials using an improved SPH model. In: *CIGOS 2019, Innovation for Sustainable Infrastructure.* Singapore: Springer; 2020:895-900.
45. Liang H, He S, Lei X, Bi Y, Liu W, Ouyang C. Dynamic process simulation of construction solid waste (CSW) landfill landslide based on SPH considering dilatancy effects. *Bull Eng Geo Environ.* 2019;78(2):763-777.
46. Nguyen CT, Nguyen CT, Bui HH, Nguyen GD, Fukagawa R. A new SPH-based approach to simulation of granular flows using viscous damping and stress regularisation. *Landslides.* 2017b;14(1):69-81.
47. Pastor M, Haddad B, Sorbino G, Cuomo S, Drempetic V. A depth-integrated, coupled SPH model for flow-like landslides and related phenomena. *Int J Numeric Analytic Meth Geomech.* 2009;33(2):143-172.
48. Pastor M, Yague A, Stickle MM, Manzanal D, Mira P. A two-phase SPH model for debris flow propagation. *Int J Numeric Analytic Meth Geomech.* 2018;42(3):418-448.
49. Zhu C, Huang Y, Zhan LT. SPH-based simulation of flow process of a landslide at Hongao landfill in China. *Nat Hazards.* 2018;93(3): 1113-1126.
50. Bui HH, Sako K, Fukagawa R, Wells JC. SPH-based numerical simulations for large deformation of geomaterial considering soil-structure interaction. In The 12th International Conference of International Association for Computer Methods and Advances in Geomechanics (IACMAG), 2008b; (Vol. 1, pp. 570-578).
51. Bui HH, Kodikara JA, Bouazza A, Haque A, Pathegama R. A novel computational approach for large deformation and post-failure analyses of segmental retaining wall systems. *Int J Numeric Analytic Meth Geomech.* 2014;38(13):1321-1340.

52. Liu M, Zhang Z. Smoothed particle hydrodynamics (SPH) for modeling fluid-structure interactions. *Sci China Phys, Mech Astro.* 2019; 62(8):984701.
53. Neto AHF, Borja RI. Continuum hydrodynamics of dry granular flows employing multiplicative elastoplasticity. *Acta Geotechnica.* 2018; 13(5):1027-1040.
54. Zhang ZL, Long T, Chang JZ, Liu MB. A smoothed particle element method (SPEM) for modeling fluid-structure interaction problems with large fluid deformations. *Comput Methods Appl Mech Eng.* 2019;356:261-293.
55. Bui HH, Sako K, Fukagawa R. Numerical simulation of soil-water interaction using smoothed particle hydrodynamics (SPH) method. *J Terramech.* 2007;44(5):339-346.
56. Bui HH, Nguyen GD. A coupled fluid-solid SPH approach to modelling flow through deformable porous media. *Int J Sol Struct.* 2017; 125:244-264.
57. Pastor M, Blanc T, Haddad B, et al. Application of a SPH depth-integrated model to landslide run-out analysis. *Landslides.* 2014;11(5): 793-812.
58. Das R, Cleary PW. Effect of rock shapes on brittle fracture using smoothed particle hydrodynamics. *Theoretic Applied Fract Mech.* 2010; 53(1):47-60.
59. Douillet-Grellier T, Jones BD, Pramanik R, Pan K, Albaiz A, Williams JR. Mixed-mode fracture modeling with smoothed particle hydrodynamics. *Comp Geotech.* 2016;79:73-85.
60. Ma GW, Wang XJ, Ren F. Numerical simulation of compressive failure of heterogeneous rock-like materials using SPH method. *Int J Rock Mech Min Sci.* 2011;48(3):353-363.
61. Monaghan JJ. SPH without a tensile instability. *J Comput Phys.* 2000;159(2):290-311.
62. Gray JP, Monaghan JJ, Swift RP. SPH elastic dynamics. *Comput Methods Appl Mech Eng.* 2001;190(49-50):6641-6662.
63. Chen JK, Beraun JE, Carney TC. A corrective smoothed particle method for boundary value problems in heat conduction. *Int J Numer Methods Eng.* 1999;46(2):231-252.
64. Dyka CT, Ingel RP. An approach for tension instability in smoothed particle hydrodynamics (SPH). *Comput Struct.* 1995;57(4):573-580.
65. Dyka CT, Randles PW, Ingel RP. Stress points for tension instability in SPH. *Int J Numer Methods Eng.* 1997;40(13):2325-2341.
66. Donea J. A Taylor-Galerkin method for convective transport problems. *Int J Numer Methods Eng.* 1984;20(1):101-119.
67. Löhner R, Morgan K, Zienkiewicz OC. The solution of non-linear hyperbolic equation systems by the finite element method. *Int J Numeric Meth Fluids.* 1984;4(11):1043-1063.
68. Blanc T, Pastor M. A stabilized smoothed particle hydrodynamics, Taylor-Galerkin algorithm for soil dynamics problems. *Int J Numeric Analytic Meth Geomech.* 2013;37(1):1-30.
69. Herreros MI, Mabssout M. A two-steps time discretization scheme using the SPH method for shock wave propagation. *Comput Methods Appl Mech Eng.* 2011;200(21-22):1833-1845.
70. Wang Y, Bui HH, Nguyen GD, Gamage RP. Numerical simulation of size effect on rock fracture using SPH and a size-dependent constitutive model. In 9th Australasian Congress on Applied Mechanics (ACAM9) 2017a; (p. 741). Engineers Australia.
71. Wang Y, Bui H, Nguyen G, Ranjith P. A mesh-free continuum based computational approach to modelling rock fracture. *Poromechanics VI.* 2017b;2041-2048.
72. Wang Y, Bui HH, Nguyen GD, Ranjith PG. A new SPH-based continuum framework with an embedded fracture process zone for modelling rock fracture. *Int J Sol Struct.* 2019;159:40-57.
73. Zhao S, Bui HH, Lemiale V, Nguyen GD, Darve F. A generic approach to modelling flexible confined boundary conditions in SPH and its application. *Int J Numeric Analytic Meth Geomech.* 2019;43:1005-1031.
74. Liu GR, Liu MB. Smoothed particle hydrodynamics: a meshfree particle method. World Scientific. 2003
75. Nguyen GD, Einav I, Korsunsky AM. How to connect two scales of behaviour in constitutive modelling of geomaterials. *Géotechnique Lett.* 2012;2(3):129-134.
76. Nguyen GD, Korsunsky AM, Einav I. A constitutive modelling framework featuring two scales of behaviour: fundamentals and applications to quasi-brittle failure. *Eng Fract Mech.* 2014;115:221-240.
77. Haghigat E, Pietruszczak S. On modeling of discrete propagation of localized damage in cohesive-frictional materials. *Int J Numeric Analytic Meth Geomech.* 2015;39(16):1774-1790.
78. Pietruszczak S, Xu G. Brittle response of concrete as a localization problem. *Int J Sol Struct.* 1995;32(11):1517-1533.
79. Pietruszczak S, Mroz Z. On failure criteria for anisotropic cohesive-frictional materials. *Int J Numeric Analytic Meth Geomech.* 2001; 25(5):509-524.
80. Xu G, Pietruszczak S. Numerical analysis of concrete fracture based on a homogenization technique. *Comput Struct.* 1997;63(3):497-509.
81. Nguyen GD, Bui HH. A thermodynamics-and mechanism-based framework for constitutive models with evolving thickness of localisation band. *Int J Sol Struct.* 2020;87:100-120.
82. Tran HT, Wang Y, Nguyen GD, Kodikara J, Sanchez M, Bui HH. Modelling 3D desiccation cracking in clayey soils using a size-dependent SPH computational approach. *Comp Geotech.* 2019;116:103209.
83. Tran HT, Bui HH, Nguyen GD, Kodikara J, Sanchez M. A continuum based approach to modelling tensile cracks in soils. *Sixth Biot Conference on Poromechanics.* 2017;337-344.
84. Le LA, Nguyen GD, Bui HH, Sheikh AH, Kotousov A, Khanna A. Modelling jointed rock mass as a continuum with an embedded cohesive-frictional model. *Eng Geo.* 2017;228:107-120.

85. Le LA, Nguyen GD, Bui HH, Sheikh AH, Kotousov A. Localised failure mechanism as the basis for constitutive modelling of geomaterials. *Int J Eng Sci.* 2018;133:284-310.
86. Le LA, Nguyen GD, Bui HH, Sheikh AH, Kotousov A. Incorporation of micro-cracking and fibre bridging mechanisms in constitutive modelling of fibre reinforced concrete. *J Mech Phys Solids.* 2019;133:103732.
87. Le LA, Nguyen GD, Bui HH. Predicting onset and orientation of localisation bands using a cohesive-frictional model. In: *CIGOS 2019, Innovation for Sustainable Infrastructure.* Singapore: Springer; 2020:311-316.
88. Belnoue JPH, Hallett SR. A rapid multi-scale design tool for the prediction of wrinkle defect formation in composite components. *Mater Des.* 2020;187:108388.
89. Kolymbas D. Kinematics of shear bands. *Acta Geotechnica.* 2009;4(4):315–318.
90. Vardoulakis I, Goldscheider M, Gudehus G. Formation of shear bands in sand bodies as a bifurcation problem. *Int J Numeric Analytic Meth Geomech.* 1978;2(2):99-128.
91. Hill R. Elastic properties of reinforced solids: some theoretical principles. *J Mech Phys Solids.* 1963;11(5):357-372.
92. Nguyen GD, Nguyen CT, Nguyen VP, Bui HH, Shen L. A size-dependent constitutive modelling framework for localised failure analysis. *Comput Mech.* 2016;58(2):257-280.
93. Bellego CL, Gérard B, Pijaudier-Cabot G. Chemo-mechanical effects in mortar beams subjected to water hydrolysis. *J Eng Mech.* 2000; 126(3):266-272.
94. Fujita Y, Ishimaru R, Hanai S, Suenaga Y. Study on internal friction angle and tensile strength of plain concrete. *Proceedings of fracture mechanics of concrete structures FRAMCOS.* 1998;3:325-334.
95. Lim IL, Johnston IW, Choi SK, Boland JN. Fracture testing of a soft rock with semi-circular specimens under three-point bending. Part 2—mixed-mode. In: *International Journal of Rock Mechanics and Mining Sciences & Geomechanics Abstracts.* 1994, June;31(3):199-212. Pergamon
96. Hoek E, Brown ET. Practical estimates of rock mass strength. *Int J Rock Mech Min Sci.* 1997;34(8):1165-1186.
97. Li DY, Tao WANG, Cheng TJ, Sun XL. Static and dynamic tensile failure characteristics of rock based on splitting test of circular ring. *Trans Nonferrous Met Soc Chin.* 2016;26(7):1912-1918.
98. Li X, Feng F, Li D. Numerical simulation of rock failure under static and dynamic loading by splitting test of circular ring. *Eng Fract Mech.* 2018;188:184-201.

**How to cite this article:** Wang Y, Tran HT, Nguyen GD, Ranjith PG, Bui HH. Simulation of mixed-mode fracture using SPH particles with an embedded fracture process zone. *Int J Numer Anal Methods Geomech.* 2020; 1–29. <https://doi.org/10.1002/nag.3069>